Available online at www.sciencedirect.com
SCIENCE DIRECT®
Astroparticle Physics 20 (2004) 507–532
Astroparticle Physics
www.elsevier.com/locate/astropart

Sensitivity of the IceCube detector to astrophysical sources of high energy muon neutrinos

J. Ahrens [a], J.N. Bahcall [b], X. Bai [c], R.C. Bay [d], T. Becka [a], K.-H. Becker [e], D. Berley [f], E. Bernardini [g], D. Bertrand [h], D.Z. Besson [i], A. Biron [g], E. Blaufuss [f], D.J. Boersma [g], S. Böser [g], C. Bohm [j], O. Botner [k], A. Bouchta [k], O. Bouhali [h], T. Burgess [j], W. Carithers [l], T. Castermans [m], J. Cavin [n], W. Chinowsky [l], D. Chirkin [d], B. Collin [o], J. Conrad [k], J. Cooley [p], D.F. Cowen [o,q], A. Davour [k], C. De Clercq [r], T. DeYoung [f], P. Desiati [p], R. Ehrlich [f], R.W. Ellsworth [s], P.A. Evenson [c], A.R. Fazely [t], T. Feser [a], T.K. Gaisser [c], J. Gallagher [u], R. Ganugapati [p], H. Geenen [e], A. Goldschmidt [l], J.A. Goodman [f], R.M. Gunasingha [t], A. Hallgren [k], F. Halzen [p], K. Hanson [p], R. Hardtke [p], T. Hauschildt [g], D. Hays [l], K. Helbing [l], M. Hellwig [a], P. Herquet [m], G.C. Hill [p], D. Hubert [r], B. Hughey [p], P.O. Hulth [j], K. Hultqvist [j], S. Hundertmark [j], J. Jacobsen [l], G.S. Japaridze [v], A. Jones [l], A. Karle [p], H. Kawai [w], M. Kestel [o], N. Kitamura [n], R. Koch [a], L. Köpke [a], M. Kowalski [g], J.I. Lamoureux [l], H. Leich [g], M. Leuthold [g], I. Liubarsky [x], J. Madsen [y], H.S. Matis [l], C.P. McParland [l], T. Messarius [e], P. Mészáros [o,q], Y. Minaeva [j], R.H. Minor [l], P. Miočinović [d], H. Miyamoto [w], R. Morse [p], R. Nahnhauer [g], T. Neunhöffer [a], P. Niessen [r], D.R. Nygren [l], H. Ögelman [p], Ph. Olbrechts [r], S. Patton [l], R. Paulos [p], C. Pérez de los Heros [k], A.C. Pohl [j], J. Pretz [f], P.B. Price [d], G.T. Przybylski [l], K. Rawlins [p], S. Razzaque [q], E. Resconi [g], W. Rhode [e], M. Ribordy [m], S. Richter [p], H.-G. Sander [a], K. Schinarakis [e], S. Schlenstedt [g], T. Schmidt [g], D. Schneider [p], R. Schwarz [p], D. Seckel [c], A.J. Smith [f], M. Solarz [d], G.M. Spiczak [y], C. Spiering [g], M. Stamatikos [p], T. Stanev [c], D. Steele [p], P. Steffen [g], T. Stezelberger [l], R.G. Stokstad [l], K.-H. Sulanke [g], G.W. Sullivan [f], T.J. Sumner [x], I. Taboada [z], S. Tilav [c], N. van Eijndhoven [aa], W. Wagner [e], C. Walck [j], R.-R. Wang [p], C.H. Wiebusch [e], C. Wiedemann [j], R. Wischnewski [g], H. Wissing [g,*], K. Woschnagg [d], S. Yoshida [w]

[*] Corresponding author. Tel.: +49-33762-77512; fax: +49-33762-77330.
E-mail address: hwissing@ifh.de (H. Wissing).

0927-6505/$ - see front matter
doi:10.1016/j.astropartphys.2003.09.003

[a] Institute of Physics, University of Mainz, Staudinger Weg 7, D-55099 Mainz, Germany
[b] Institute for Advanced Study, Princeton, NJ 08540, USA
[c] Bartol Research Institute, University of Delaware, Newark, DE 19716, USA
[d] Department of Physics, University of California, Berkeley, CA 94720, USA
[e] Fachbereich 8 Physik, BUGH Wuppertal, D-42097 Wuppertal, Germany
[f] Department of Physics, University of Maryland, College Park, MD 20742, USA
[g] DESY-Zeuthen, D-15738 Zeuthen, Germany
[h] Université Libre de Bruxelles, Science Faculty CP230, Boulevard du Triomphe, B-1050 Brussels, Belgium
[i] Deparment of Physics and Astronomy, University of Kansas, Lawrence, KS 66045, USA
[j] Department of Physics, Stockholm University, SE-10691 Stockholm, Sweden
[k] Division of High Energy Physics, Uppsala University, S-75121 Uppsala, Sweden
[l] Lawrence Berkeley National Laboratory, Berkeley, CA 94720, USA
[m] University of Mons-Hainaut, 7000 Mons, Belgium
[n] SSEC, University of Wisconsin, Madison, WI 53706, USA
[o] Department of Physics, Pennsylvania State University, University Park, PA 16802, USA
[p] Department of Physics, University of Wisconsin, Madison, WI 53706, USA
[q] Department of Astronomy and Astrophysics, Pennsylvania State University, University Park, PA 16802, USA
[r] Vrije Universiteit Brussel, Dienst ELEM, B-1050 Brussels, Belgium
[s] Department of Physics, George Mason University, Fairfax, VA 22030, USA
[t] Department of Physics, Southern University, Baton Rouge, LA 70813, USA
[u] Department of Astronomy, University of Wisconsin, Madison, WI 53706, USA
[v] CTSPS, Clark-Atlanta University, Atlanta, GA 30314, USA
[w] Department of Physics, Chiba University, Chiba 263-8522, Japan
[x] Blackett Laboratory, Imperial College, London SW7 2BW, UK
[y] Department of Physics, University of Wisconsin, River Falls, WI 54022, USA
[z] Departamento de Física, Universidad Simón Bolívar, Caracas, 1080, Venezuela
[aa] Faculty of Physics and Astronomy, Utrecht University, NL-3584 CC Utrecht, The Netherlands

Received 6 June 2003; received in revised form 27 August 2003; accepted 15 September 2003

Abstract

We present results of a Monte Carlo study of the sensitivity of the planned IceCube detector to predicted fluxes of muon neutrinos at TeV to PeV energies. A complete simulation of the detector and data analysis is used to study the detector's capability to search for muon neutrinos from potential sources such as active galaxies and gamma-ray bursts (GRBs). We study the effective area and the angular resolution of the detector as a function of muon energy and angle of incidence. We present detailed calculations of the sensitivity of the detector to both diffuse and pointlike neutrino fluxes, including an assessment of the sensitivity to neutrinos detected in coincidence with GRB observations. After three years of data taking, IceCube will be able to detect a point-source flux of $E_\nu^2 \times \mathrm{d}N_\nu/\mathrm{d}E_\nu = 7 \times 10^{-9}$ cm^{-2} s^{-1} GeV at a 5σ significance, or, in the absence of a signal, place a 90% c.l. limit at a level of $E_\nu^2 \times \mathrm{d}N_\nu/\mathrm{d}E_\nu = 2 \times 10^{-9}$ cm^{-2} s^{-1} GeV. A diffuse E^{-2} flux would be detectable at a minimum strength of $E_\nu^2 \times \mathrm{d}N_\nu/\mathrm{d}E_\nu = 10^{-8}$ cm^{-2} s^{-1} sr^{-1} GeV. A GRB model following the formulation of Waxman and Bahcall would result in a 5σ effect after the observation of 200 bursts in coincidence with satellite observations of the gamma rays.

PACS: 95.55.Vj; 95.85.Ry
Keywords: Neutrino telescope; Neutrino astronomy; IceCube

1. Introduction

The emerging field of high-energy neutrino astronomy [1–3] has seen the construction, operation and results from the first detectors, and proposals for the next generation of such instruments. The pioneering efforts of the DUMAND [4] collaboration were followed by the successful

deployments of NT-200 at Lake Baikal [5] and AMANDA [6] at the South Pole. These detectors have demonstrated the feasibility of large neutrino telescopes in open media like sea- or lake-water and glacial ice. They have been used to observe neutrinos produced in the atmosphere [7] and to set limits on the flux of extraterrestrial neutrinos [8,9] which are significantly below those obtained from the much smaller underground neutrino detectors [10,46]. The results obtained so far, together with refinements of astrophysical theories predicting extraterrestrial neutrino fluxes from cosmic sources, have provided the impetus to construct a neutrino observatory on a much larger scale. Proposals for a detector in the deep water of the Mediterranean have come from the ANTARES [11], NESTOR [12] and NEMO [13] collaborations. IceCube is a projected cubic-kilometer under-ice neutrino detector [14–16], to be located near the geographic South Pole in Antarctica.

The IceCube detector will consist of optical sensors deployed at depth into the thick polar ice sheet. The ice will serve as Cherenkov medium for secondary particles produced in neutrino interactions in or around the instrumented volume. The successful deployment and operation of the AMANDA detector have shown that the polar ice is a suitable medium for a large neutrino telescope and the analysis of AMANDA data has proven the science potential of such a detector.

IceCube will offer great advantages over AMANDA beyond its larger size: it will have a higher efficiency and a higher angular resolution in reconstructing muon tracks, it will map electromagnetic and hadronic showers (*cascades*) from electron- and tau-neutrino interactions and, most importantly, it will have a superior energy resolution. Simulations, backed by AMANDA data, indicate that the direction of muons can be determined with subdegree accuracy and their energy measured to better than 30% in the logarithm of the energy. For electron neutrinos that produce electromagnetic cascades, the direction can be reconstructed to better than 25° and the response in energy is linear with a resolution better than 10% in the logarithm of the energy [16]. Good energy resolution is crucial in that it allows full sky coverage for ultrahigh-energy extraterrestrial neutrinos, since no atmospheric muon or neutrino background exceeds 1 PeV in a deep, cubic-kilometer detector.

IceCube will be able to investigate a large variety of scientific questions in astronomy, astrophysics, cosmology and particle physics [16,22]. In this paper we focus on the IceCube performance in searching for TeV to PeV muon neutrinos, as expected from sources such as active galactic nuclei (AGN), gamma-ray bursts (GRBs) or other cosmic accelerators observed as TeV gamma-ray emitters. We present the results of a Monte Carlo study that includes the simulation of the detector and the full analysis chain, from filtering of the triggered data to event reconstruction and selection. We assess basic detector parameters, such as the pointing resolution and the effective area of the detector, directly from simulated data. We also present a detailed calculation of the detector's sensitivity to both diffuse and pointlike neutrino emission following generic energy spectra, providing benchmark sensitivities for some of the fundamental goals in high-energy neutrino astronomy.

2. The IceCube detector

The IceCube detector is planned as a cubic-kilometer-sized successor to the AMANDA detector. It will consist of 4800 photomultiplier tubes (PMTs) of 10-inch diameter, each enclosed in a transparent pressure sphere. These optical modules (OMs) will be arrayed on 80 cables, each such *string* comprising 60 modules spaced by 17 m. During deployment the strings will be lowered into vertical, water-filled holes, drilled to a depth of 2400 m with pressurized hot water, and allowed to freeze in place. The instrumented volume will span a depth from 1400 to 2400 m below the ice surface. In the horizontal plane the strings will be arranged in a triangular pattern such that the distances between each string and its up-to-six nearest neighbors are 125 m (Fig. 1). This configuration is the result of an extensive optimization procedure [18,19].

The relatively sparse instrumentation is made possible by the low light absorption of the deep Antarctic ice. The absorption length for light from

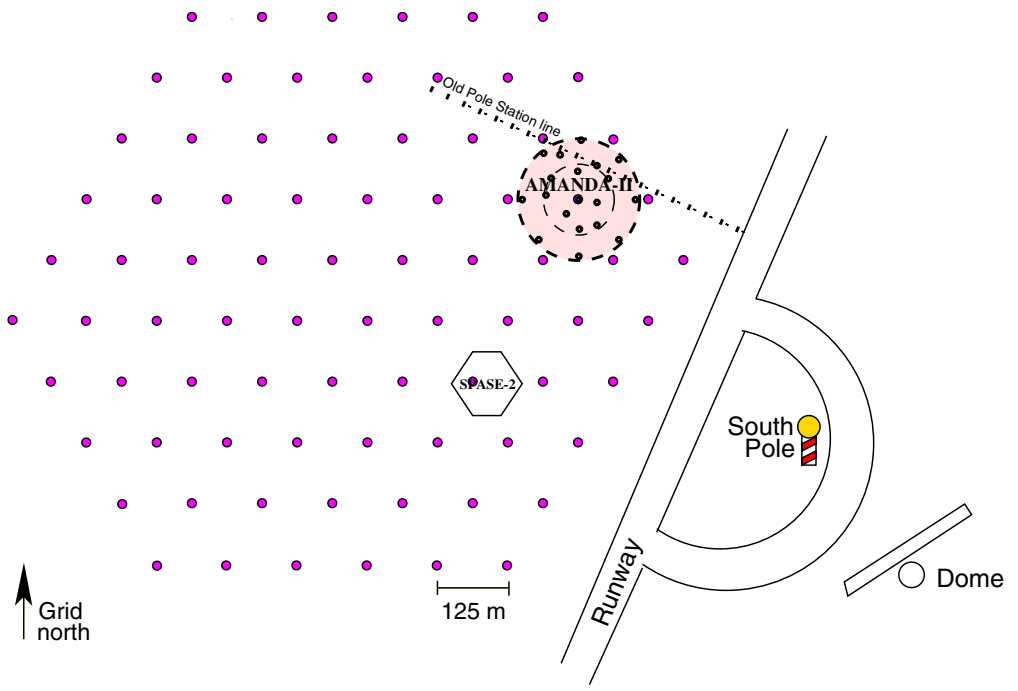

Fig. 1. Schematic view of the planned arrangement of strings of the IceCube detector at the South Pole station. The existing AMANDA-II detector will be embedded in the new telescope, and the SPASE-2 air-shower array will lie within its horizontal boundaries.

UV to blue varies between 50 and 150 m, depending on depth. Light scattering, on the other hand, will result in strong dispersion of the Cherenkov signal over large distances, diluting the timing information carried by the photons. This scattering effect increases with the average distance at which photons are collected, but is somewhat compensated for by the information contained in the time structure of the recorded PMT pulse, since, e.g., its length is a measure for the distance to the point of light emission.

As a significant improvement over the AMANDA technology, each IceCube OM will house electronics to digitize the PMT pulses, so that the full waveform information is retained [17]. The waveforms will be recorded at a frequency of about 300 mega-samples per second, leading to an intrinsic timing accuracy for a single pulse measurement of 7 ns. The digitized signals will be transmitted to the data acquisition system, located at the surface, via twisted-pair cables. Each OM will communicate, through an embedded CPU, with its nearest neighbors by means of a dedicated copper-wire pair. This enables the implementation of a local hardware trigger in the ice, such that digitization occurs only when some coincidence requirement has been met [16]. This is particularly important in order to suppress the transmission of pure noise pulses, which, unlike photon pulses from high-energy particles, are primarily isolated, i.e., occur without correlation to pulses recorded in neighboring and nearby OMs. (The dark noise rate of an OM will be as low as 300–500 Hz, due to the sterile and low-temperature environment.) Local triggers will be combined by surface processors to form a global trigger. Triggered events will be filtered and reconstructed on-line, and the relevant information will be transmitted via satellite to research institutions in the northern hemisphere.

The complete detector will be operational perhaps as soon as five years after the start of construction, but during the construction phase all deployed strings will already produce high-quality data.

The IceCube array deep in the ice will be complemented by IceTop, a surface air-shower array consisting of 160 frozen-water tanks. The tanks will be arranged in pairs, separated by a few meters, one on top of each IceCube string. IceTop is the logical extension of the SPASE surface array [20] which already is a unique asset for AMANDA. The air-shower parameters measured at the surface combined with the signal from the high-energy muon component at depth provide a new measure for the primary composition of cosmic rays. Furthermore, data from IceTop will serve as a veto for air-shower-induced background and will enable cross-checks for the detector geometry calibration, absolute pointing accuracy and angular resolution. In addition, the energy deposited by tagged muon bundles in air-shower cores will be an external source for energy calibration.

3. Simulation and analysis chain

The science potential of a kilometer-scale neutrino telescope has been assessed in previous papers by convoluting the expected neutrino-induced muon flux from various astrophysical sources with an assumed square-kilometer effective detector area [21–23]. In this work we use a full simulation of event triggering, reconstruction and data selection to assess the detector capabilities. The simulation of the detector response and the analysis of Monte Carlo-generated data rely on software packages presently provided by the AMANDA collaboration [24,40]. This means that the software concepts and analysis techniques used here have proven capable and have been verified by real data taken with the AMANDA detector. However, a full simulation of the IceCube hardware was not possible with the present software. The simulated data correspond to the original AMANDA readout, which does not yield full waveforms for the PMT pulses, but only leading-edge times and peak amplitudes (of which only the timing information is used in the reconstruction). More advanced analysis methods which take advantage of the additional information were not applied and hence this work may yield a conservative assessment of the IceCube performance.

3.1. Event generation

The backgrounds for searches for extraterrestrial neutrinos come from the decay of mesons produced from cosmic-ray interactions in the atmosphere. The decay products include both muons and neutrinos. The muons created above the detector will be responsible for the vast majority of triggers, since they are sufficiently penetrating to be capable of reaching the detector depth. Air-shower-induced events can be identified by the fact that they involve exclusively downward tracks and a comparatively small deposit of Cherenkov light in the detector, as the muons will have lost most of their energy upon reaching the detector. However, an upward track might be faked if two uncorrelated air showers produce time-coincident muons within the detector. About three percent of all triggered events will be caused by muons from two independent air showers.

The simulation packages `Basiev` [25] and `Corsika` [26] were used to generate cosmic-ray-induced muon background. Roughly 2.4 million events containing muon tracks from one single air shower ($Atm\ \mu^{\mathrm{single}}$) were simulated with primary energies up to 10^8 GeV. High-energy events and events containing tracks close to the horizon were oversampled, in order to achieve larger statistics at high analysis levels. In addition, we simulated one million events containing tracks from two independent air showers ($Atm\ \mu^{\mathrm{double}}$).

Muons induced by atmospheric neutrinos ($Atm\ \nu$) form a background over the full sky and up to very high energies. However, the energy spectrum of atmospheric neutrinos falls steeply like $\mathrm{d}N_\nu/\mathrm{d}E_\nu \propto E_\nu^{-3.7}$, whereas one expects an energy spectrum as hard as E^{-2} from shock-acceleration mechanisms in anticipated cosmic TeV-neutrino sources. Therefore, cosmic-neutrino energies should extend to higher values and cause more light in the detector than will atmospheric neutrinos. The amount of light observed in an event is therefore useful as a criterion to separate high-energy muons induced by cosmic neutrinos from those induced by atmospheric neutrinos. An uncertainty in the flux of atmospheric neutrinos at high energies arises from the poorly known

contribution from prompt decays of charmed mesons produced in the atmosphere. The prompt-charm-related muon-neutrino fluxes predicted by various theoretical models [27,28] show large variations. Most of the uncertainty is associated with the extrapolation of charm-production models to high energies. Models applying perturbative QCD, for example, predict higher fluxes than non-perturbative QCD approaches.

Neutrino-induced events were simulated with the program `nusim` [29], which allows the generation of muon neutrinos with arbitrary energy spectra. Neutrinos are sampled from an E^{-1} spectrum and are then reweighted to produce user-defined energy spectra, as required. The code includes a simulation of neutrino propagation through the Earth, taking into account absorption in charged-current interactions as well as neutral-current regeneration. The neutrino cross sections are calculated using the MRSG [30] parton distributions. The column density of nucleons to be traversed is calculated according to the Preliminary Reference Earth Model [31]. Muons that are produced in the rock beneath the detector are propagated to the rock/ice boundary using the Lipari–Stanev [32] muon propagation code. In total, we simulated 7.4×10^5 events induced by neutrinos with primary energies up to 10^8 GeV. The flatness of the generated E^{-1} neutrino spectrum leads to a statistically beneficial oversampling of events at high energies for the mostly softer energy spectra investigated.

For the "conventional" flux of atmospheric neutrinos (i.e., the component related to decays of pions and kaons) we apply the prediction calculated by Lipari [33]. For the prompt-charm contribution we compare the predictions from two different charm-production models: a phenomenological non-perturbative approach, the Recombination Quark Parton Model (`rqpm`), by Bugaev et al. [34], and perturbative QCD calculations made by Thunman et al. (`TIG`) [35]. The prompt-neutrino event rate predicted by `TIG` is the lower by more than an order of magnitude, and is low even when compared to other calculations using non-perturbative QCD (e.g., [36]), and may therefore serve as a lower limit for the prompt-charm contribution.

For the flux of extraterrestrial neutrinos (*Cosmic ν*) we apply a generic E^{-2} energy spectrum, as expected from shock acceleration. We use a source strength of $E_\nu^2 \times \mathrm{d}N_\nu/\mathrm{d}E_\nu = 10^{-7}\ \mathrm{cm}^{-2}\,\mathrm{s}^{-1}\,\mathrm{sr}^{-1}$ GeV as a benchmark diffuse flux of extraterrestrial neutrinos. This is the logarithmic mean of two upper bounds on the diffuse neutrino flux: (a) the bound obtained if one assumes that the neutrino sources are completely transparent to neutrons and that these sources are responsible for the observed flux of ultrahigh-energy cosmic rays, while one does not allow for cosmological evolution of the sources, and (b) the bound obtained if one assumes that the sources are opaque to neutrons and only high-energy gamma rays escape ([2] and references therein). The flux is an order of magnitude below present experimental limits set on the flux of muon neutrinos [9] and electron neutrinos [37].

3.2. Muon propagation

The propagation of muons through the ice is modeled with either the code by Lohmann et al. [38] (for muon energies smaller than $10^{5.5}$ GeV) or the code by Lipari and Stanev [32] (for muon energies greater than $10^{5.5}$ GeV). These codes calculate the stochastic-radiative and nuclear-interactive energy losses along the muon track within or close to the instrumented detector volume.

The complete tracking of all Cherenkov photons produced by the muon and associated stochastic-radiative energy losses for each event would require an impractical amount of computing power. Therefore, the photon amplitudes and timing distributions at all points in space from both a muon and an electromagnetic cascade are pre-calculated and tabulated for fast lookup using the `PTD` [39] software package. This simulation takes into account the scattering and absorption properties of the ice as well as the response of the PMT.

3.3. Detector simulation

The response of the entire array of optical modules is modeled with the detector simulation

amasim [40,41]. The actual number of photons at an OM is found by sampling from a Poisson distribution with a mean amplitude computed by summing over all contributing muons and cascades. The arrival times of these photons are sampled from the pre-tabulated distributions. Noise pulses are added assuming a PMT noise rate of 500 Hz. For event triggering, and to suppress PMT noise, we require at least five local coincidences in a global trigger time window of 7 μs. A local coincidence is defined as the registration of at least two pulses within 1 μs among an OM and its nearest and next-to-nearest neighbors. Only pulses that are part of a local coincidence are read out and used for further reconstruction.

The detector geometry used in this simulation differs from the finalized design in the total number of strings (we have simulated a detector with 75 strings instead of 80), the total number of OMs (4575 instead of 4800), the instrumented string length (960 m instead of 1000 m) and the depth of the detector center (which was simulated at 2000 m, while it will lie at 1900 m in the updated design). The spatial arrangement with the strings spaced 125 m apart on a triangular grid is in accordance with the design presented in the previous section. A simulation of the detector in its finalized configuration using a subsample of the Monte Carlo-generated events showed an increase in the expected event rates of roughly 10% for both signal and background at trigger level.

3.4. Event reconstruction

The reconstruction of an event involves fitting a muon track hypothesis to the recorded pattern of PMT pulses (“hits”) assumed to be caused by Cherenkov photons generated by the muon. Triggered events are first reconstructed with three fast “first guess” algorithms which use the arrival times of the photons or the topology of OMs having registered a hit: (1) The *line fit* (LF) is based on a simple analytic χ^2 minimization [42]. It fits the free parameters (vertex position and velocity) of a hypothetical straight-line trajectory to the one-dimensional projection of the observed pattern of hits. (2) The *dipole approximation* [43] is based on the hit topology. The sum of all unit vectors pointing from one hit to the next in time gives a “dipole vector” $\vec{M}$. The direction of $\vec{M}$ is correlated to the direction of the incoming track(s), while its absolute value is a measure of the goodness of the approximation. (3) The *direct walk algorithm* (DW) [43] posits as track hypotheses the straight-line connections between every pair of hits that have occurred in separate OMs with a time difference consistent with the muon flight time between these two OMs. Those track hypotheses that pass a consistency check with respect to the complete hit pattern of the event are combined to obtain an estimate of the track parameters.

Following these first-guess methods, the events are reconstructed using a full *maximum likelihood reconstruction* (LR) [43,44]. The probabilities in the likelihood function are based on the arrival-time distribution of photons emitted along a track as a function of distance and angle of the track with respect to the OM. These distributions have been obtained from a detailed photon-propagation simulation. The reconstruction used here relies only on the timing information carried by the *first* photon that is recorded by the OM. This corresponds to the current practice in AMANDA, whose original read-out only yields minimal timing information for the pulses (leading and trailing edges at the corresponding threshold crossings) and the peak amplitude seen by the PMT in the event. [1]

4. Basic performance capabilities

The trigger rate for a fivefold local coincidence trigger was found to be 1.7 kHz. This includes a 50 Hz rate of triggers due to uncorrelated time-coincident air showers ($Atm\ \mu^{\mathrm{double}}$). As described below, a set of event selection criteria

[1] In contrast, the IceCube electronics will retain the full pulse shape. Detailed hit information can then be extracted from the integrated charge and the peak structure of the pulse. Future reconstructions will therefore profit from the additional information carried by consecutively arriving photons which were multiple-scattered and delayed on their way from the muon track to the PMT.

was established that removes the bulk of the downward cosmic-ray-induced muons, but still yields a high passing rate for upward muons from atmospheric neutrinos. These atmospheric-neutrino events would then form the main background in searches for cosmic neutrinos. We use this level of data reduction as a baseline performance measure.

4.1. Event selection

The most effective handle to reject the background of downward cosmic-ray-induced muons is provided by the zenith angles [2] obtained from the various reconstruction and filter algorithms (Θ_{LR}, Θ_{LF}, Θ_{DW} and $\Theta_{\tilde{M}}$). The most straightforward way to reject cosmic-ray muons would be to exclusively select upward tracks. However, muons from PeV or EeV neutrino interactions are expected to arrive from directions close to or above the horizon, so it is worthwhile to combine the angular cut with an energy criterion. If the neutrino interaction occurs close to the detector, the energy deposit of the daughter muon will be large enough to distinguish it from low-energy cosmic-ray muons. An estimator of this energy deposit is the number of OMs (or "channels") that have registered a hit. We therefore accept downward tracks provided the channel multiplicity, N_{ch}, of the event is sufficiently large.

The selection criteria used in the data reduction are listed in Table 1. The first three criteria are based on the estimates of track directions obtained from the three first-guess methods and aim at the early rejection of low-energy downward cosmic-ray muons. The level of data reduction achieved with the application of cuts 1–3 will be referred to as "level 1".

The higher "level 2", defined by cuts 4–9, is based on variables from the more accurate (and more CPU intensive) LR:

- Events reconstructed with zenith angles smaller than 85° (i.e., directions more than 5° above the horizon) are rejected, as long as N_{ch} is less than 150. The N_{ch} criterion is tightened with decreasing zenith angle (Θ_{LR}) [cut 4].

Apart from the direction criterion, the LR provides a series of quality parameters, which we apply cuts on in order to select a sample of high-quality and well-reconstructed events:

- We require the *reduced likelihood* ($\mathscr{L}$) to be sufficiently small. $\mathscr{L}$ is given by the negative logarithm of the likelihood of the best-fit track hypothesis divided by the number of degrees of freedom of the fit, hence a *small* value indicates a good track quality [cut 5].
- We require a minimum *number of direct hits* (N_{direct}), i.e., hits that have occurred with a relatively short delay (<150 ns) relative to the arrival time predicted for an unscattered Cherenkov photon emitted from the reconstructed track [cut 6].
- We require a minimum *track length* (L), i.e., a minimum distance along the reconstructed track over which the hits were detected. We define this length as the maximum distance between two hit positions projected on the straight line defining the track direction. A more stringent criterion is a lower bound on the track length based only on direct hits (L_{direct}) [cut 7].
- The consistency of the fitted track direction is checked with the *smoothness parameter* [7,43]. It is a measure of the evenness of the projection of the hit positions along the track, based on a Kolmogorov–Smirnov test. The smoothness parameter is calculated both with all hits (S) and exclusively with direct hits (S_{direct}) [cut 8].
- For high-quality tracks, the various reconstruction methods are likely to produce similar results close to the true track direction. We therefore require the difference in zenith angles obtained by two different methods to be small [cuts 9 and 3].

These quality criteria are particularly important for muons that travel merely a short distance through the instrumented detection volume, e.g.,

[2] The detector coordinate system is oriented such that a zenith angle of $\Theta = 0°$ corresponds to vertically downward-going tracks, and, correspondingly, tracks from straight below the detector have $\Theta = 180°$.

Table 1
Definitions of individual cuts and cut levels

	Parameter	Cut	Explanation
Level 1			
1.	Θ_{LF}	$> 60°$ if $N_{\mathrm{ch}} < 50$	Zenith-angle criterion based on LF, applied for low-multiplicity events
2.	$\Theta_{\vec{M}}$	$> 50°$ if $\lvert\vec{M}\rvert > 0.2$	Zenith-angle criterion based on $\vec{M}$, applied for high goodness-of-fit values
3.	$\lvert\Theta_{\mathrm{DW}} - \Theta_{\vec{M}}\rvert$	$< 50°$	Consistency of LF and DW
Level 2			
4.	Θ_{LR}	$>85°$ *or* $N_{\mathrm{ch}} > 150 + 250 \cdot \cos\Theta_{\mathrm{LR}}$	Zenith-angle criterion of LR which is weakened with increasing channel multiplicity
5.	$\mathscr{L}$	<10	Reduced likelihood of LR
6.	N_{direct}	>10 if $N_{\mathrm{ch}} < 50$	Requirement of 10 direct hits for low-multiplicity events
7.	L L_{direct}	>300 m *and* >300 m if $N_{\mathrm{ch}} < 150$	Requirement of minimum track length, using direct hits for multiplicities smaller than 150
8.	$\lvert S\rvert$ $\lvert S_{\mathrm{direct}}\rvert$	<0.5 *and* <0.5 if $N_{\mathrm{ch}} < 50$	Constancy of light output along the track, requirement is tightened for low multiplicities
9.	$\lvert\Theta_{\mathrm{LF}} - \Theta_{\mathrm{LR}}\rvert$	$<10°$ if $N_{\mathrm{ch}} < 150$	Consistency of LF and LR

Cut level 1 uses the "first-guess" zenith angles Θ_{LF}, $\Theta_{\vec{M}}$ and Θ_{DW} as obtained from the *linefit*, the *dipole approximation* and the DW algorithm. Level 2 exploits the fitted zenith angle from the *LR*, Θ_{LR}, and various quality parameters from the fit, such as the reduced likelihood $\mathscr{L}$, the number of unscattered photons N_{direct}, the track length L (L_{direct}) defined as the maximum distance between the positions of two (direct) hits projected on the track, the *smoothness* parameters S and S_{direct} which are a measure of the evenness of the light emission along the track and the difference between the zenith angles Θ_{LF} and Θ_{LR}. Most of the cuts are varied with the number of modules (or channels), N_{ch}, that have recorded at least one hit in the event. A zenith angle of $\Theta = 0°$ corresponds to a vertically downward-going track.

low-energy muons or muons that pass only through the rim of the detector or even outside its geometrical volume. These muons will cause hits in fewer OMs and therefore provide less information for the reconstruction. Most of the quality criteria are therefore tightened if N_{ch} is small.

4.2. Muon detection rates

We compare the detector response as well as the event selection efficiency for all types of events: cosmic-ray muons, muons induced by atmospheric neutrinos and muons from cosmic neutrinos with a hard energy spectrum, following an E^{-2} power law. The numbers of triggered and selected events at each level, normalized to one year of data taking, are listed in Table 2. With a flux of $E_\nu^2 \times \mathrm{d}N_\nu/\mathrm{d}E_\nu = 10^{-7}\ \mathrm{cm}^{-2}\,\mathrm{s}^{-1}\,\mathrm{sr}^{-1}\,\mathrm{GeV}$ adopted as a benchmark for the flux of cosmic neutrinos, we expect more than 1000 signal events per year at level 2. At this level, both the background from atmospheric neutrinos and the background from cosmic-ray muons yield roughly 10^5 events per year. The `rqpm` model for atmospheric charm predicts a contribution of almost 5000 prompt-charm events to the atmospheric background. The `TIG` model predicts thirty times fewer events.

Fig. 2 shows distributions of the reconstructed zenith angle, Θ_{LR}, for the four event classes (*Cosmic ν*, *Atm ν*, *Atm* μ^{single} and *Atm* μ^{double}) at different cut levels. The level 1 selection removes the bulk of low-energy downward cosmic-ray-induced background. The cuts on the zenith angles from the first-guess methods being relatively soft, most of the remaining background is located in the angular region around 30° above the horizon

Table 2
Passing rates for signal and background events predicted for one year of data

	Trigger	Level 1	Level 2
Cosmic ν	3331 ± 6	2172 ± 4	1089 ± 3
Atm ν	$(824 \pm 4) \times 10^3$	$(264 \pm 2) \times 10^3$	$(91 \pm 1) \times 10^3$
TIG	$(0.97 \pm 0.003) \times 10^3$ [0.1%]	$(0.40 \pm 0.002) \times 10^3$ [0.2%]	$(0.17 \pm 0.001) \times 10^3$ [0.2%]
rqpm	$(24.8 \pm 0.07) \times 10^3$ [3%]	$(11.08 \pm 0.04) \times 10^3$ [4%]	$(4.85 \pm 0.03) \times 10^3$ [5%]
Atm μ^{single}	$(5.2 \pm 0.01) \times 10^{10}$	$(1.3 \pm 0.01) \times 10^9$	$(72 \pm 3) \times 10^3$
Atm μ^{double}	$(1.6 \pm 0.02) \times 10^9$	$(4.6 \pm 0.3) \times 10^7$	$(28 \pm 7) \times 10^3$

The signal expectation corresponds to a source flux of $E_\nu^2 \times \mathrm{d}N_\nu/\mathrm{d}E_\nu = 10^{-7}$ cm^{-2} s^{-1} sr^{-1} GeV. The expectation for atmospheric-neutrino events is listed separately for the "conventional" component and the "prompt" component (following [35] (TIG) and [34] (rqpm)). The fraction of prompt-charm events with respect to the whole atmospheric-neutrino sample is given in square brackets. The numbers of cosmic-ray muon background events are shown separately for events that contain muon(s) from only one air shower (*Atm* μ^{single}) and those that contain muons from two accidentally coinciding air showers (*Atm* μ^{double}). The quoted uncertainties are statistical only.

($\cos\Theta_{\text{LR}} \approx 0.5$). Level 2 then restricts the allowed zenith region to less than 5° above the horizon, except for very bright (i.e., high-multiplicity) events. The remaining ordinary cosmic-ray muon background (*Atm* μ^{single}) at level 2 is concentrated at the horizon and could be rejected with a tightened cut on the zenith angle, while the sample of cosmic-ray-induced background composed of muons from two air showers (*Atm* μ^{double}) still contains misreconstructed events that "fake" an upward-going track. However, level 2 does not contain a definite energy discrimination, required to separate the high-energy signal of cosmic neutrinos from the atmospheric-neutrino background. In the simplest approach this energy selection is accomplished by an additional tight cut on the channel multiplicity. This final cut, which has to be optimized for different analysis purposes (see Section 5.2), will lead to a drastic reduction of all three classes of background. In this analysis, none of the cosmic-ray muon events passed this additional N_{ch} cut.

Simulated energy spectra for muons generated by cosmic and atmospheric neutrinos are shown in Fig. 3. At the point of their closest approach to the detector center, muons from a cosmic E^{-2} neutrino source typically have energies in the TeV–PeV range, whereas the energy distribution for the background of muons induced by atmospheric neutrinos peaks between 100 and 300 GeV. Fig. 4 shows channel-multiplicity distributions at level 2 for all event classes. The signal class of high-energy cosmic neutrinos shows a clear excess at high multiplicities compared to the lower-energy background classes.

4.3. Effective detector area

As a measure of the detector efficiency we use the effective detector area, defined as

$$A_{\text{eff}}(E_\mu, \Theta_\mu) = \frac{N_{\text{detected}}(E_\mu, \Theta_\mu)}{N_{\text{generated}}(E_\mu, \Theta_\mu)} \times A_{\text{gen}}, \tag{1}$$

where N_{detected} is the number of events that trigger the detector or pass the cut level under consideration, from a test sample of $N_{\text{generated}}$ muons that have an energy E_μ at a given point within the fiducial volume and an incident zenith angle Θ_μ. In the following, we give E_μ at the point of closest approach to the detector center (which might lie outside the geometrical detector volume). The fraction of generated to triggered or selected events is scaled with the size of the generation plane, A_{gen}, which is the cross-sectional area of the cylinder that contains all generated muon tracks with directions parallel to its axis.

The effective area will depend on the muon energy, since very bright high-energy muons will trigger the detector and pass the selection criteria more efficiently. It will also depend strongly on the zenith angle of the incident muon after event selection, since low-energy muons are always re-

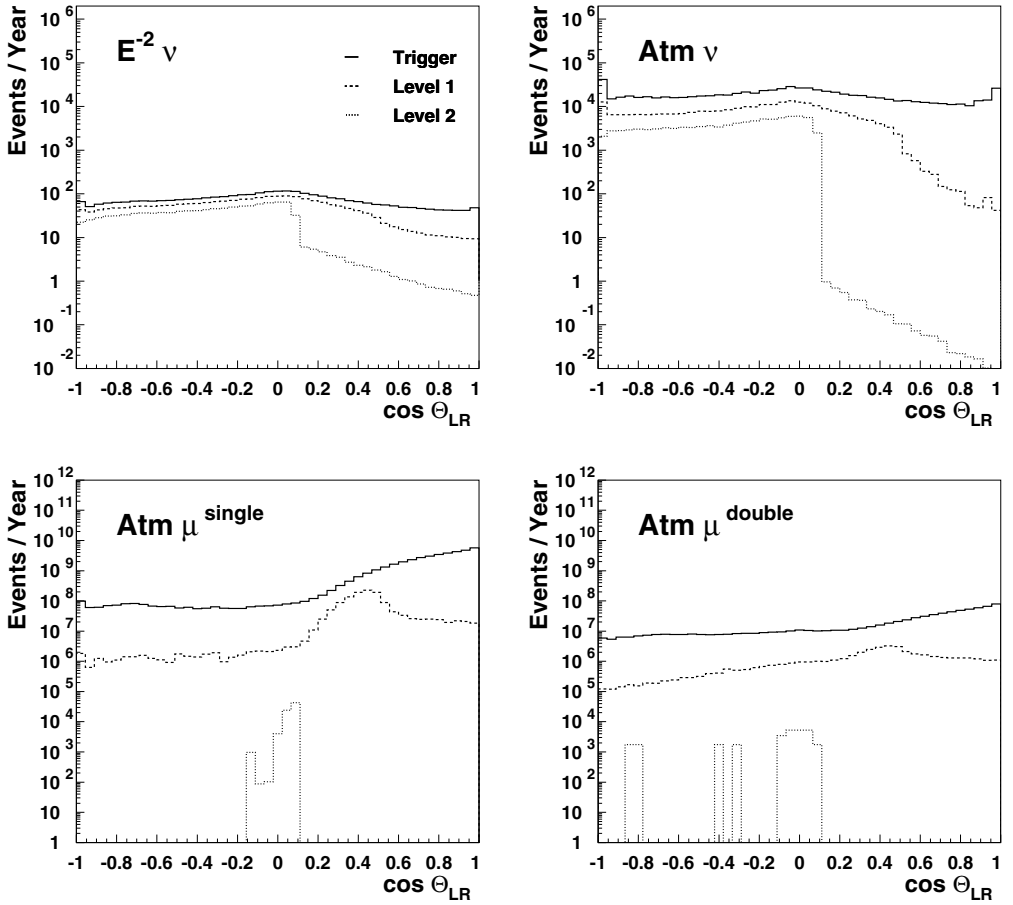

Fig. 2. *Reconstructed zenith angle* for signal from a diffuse flux of cosmic neutrinos following an E^{-2} spectrum of intensity $E_\nu^2 \times dN_\nu/dE_\nu = 10^{-7}$ cm^{-2} s^{-1} sr^{-1} GeV (top left), atmospheric neutrino background including `rqpm` charm according to [34] (top right), and atmospheric muon background from single air showers (bottom left) and from two coincident air showers (bottom right). The individual histograms in each plot correspond to trigger level (solid lines) and after applying level 1 (dashed lines) and level 2 (dotted lines) cuts. Event numbers are normalized to one year. The irregular shapes of the level 2 distributions in the lower plots are due to the low number of events (before normalization) remaining in the simulated samples at this level.

jected if they arrive from above the horizon. Thus, the effective area for a neutrino telescope, as it is defined here, is a priori zero for downward events below a certain energy.

In order to expose only the *energy* dependence of the trigger- and selection efficiencies, we have computed A_{eff} using a sample of muons which arrive from below the horizon, i.e., tracks with incident zenith angles larger than 90° (or $\cos\Theta_\mu < 0$). This has the advantage that the angular cuts, which reject low-multiplicity downward muons, have no impact on the signal (except for completely misreconstructed events) and so the efficiency is not artificially reduced by the "blindness" of the experiment to low-energy muons from the southern sky. Fig. 5 shows the effective area as a function of the muon energy for muons arriving from the northern sky. At trigger level the detector shows a sizeable acceptance even for low-energy events. The effective trigger area reaches one square kilometer at a few hundred GeV. Sensitivity to sub-TeV signals is required for science missions like the search for weakly interacting massive particles (WIMPs). WIMPs might be trapped in

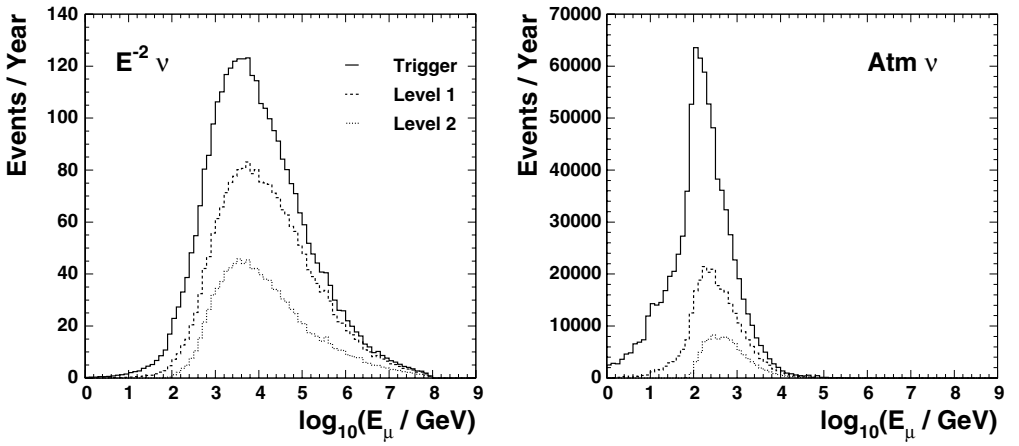

Fig. 3. *Energy spectra for neutrino-induced muons at different cut levels* for signal from an E^{-2} source (left) and atmospheric neutrino background (right). Each plot shows the muon energy at the point of closest approach to the detector center and compares the spectra at trigger level (solid lines) and after applying level 1 (dashed lines) and level 2 (dotted lines) cuts.

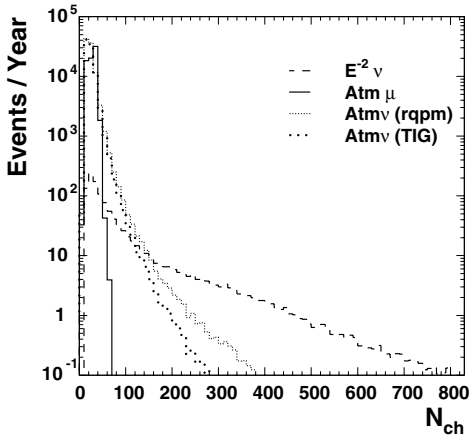

Fig. 4. *Channel multiplicity at level 2* for signal from an E^{-2} source (dashed), atmospheric neutrinos including the two alternative charm contributions `TIG` (sparse dots) and `rqpm` (dense dots) and cosmic-ray muon events (solid).

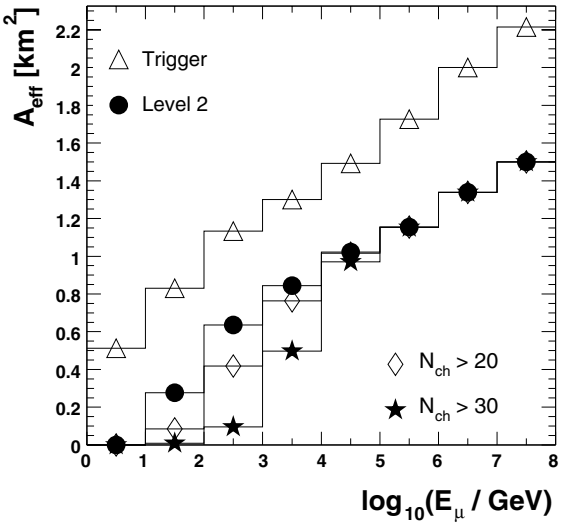

Fig. 5. *Effective area as a function of the muon energy* at trigger level, after level 2 selection and after additional energy-sensitive cuts on the number of channels (N_{ch}) that have recorded at least one hit. The effective area was calculated using a muon sample with arrival directions from the northern sky only, meaning that the data points reflect an average over one hemisphere.

the center of the Earth where they can annihilate pairwise, producing muon neutrinos that can be detected by IceCube. A dedicated selection, tailored to select vertical, upward-going tracks, could retain most of the triggered signal in the GeV range [16].

The search for high-energy extraterrestrial neutrinos, on the other hand, would benefit from a raised energy threshold, as the signal-to-background ratio improves with increased energy. The optimal threshold, i.e., the threshold that maximizes the sensitivity to a given signal, is determined by the shape of the signal energy spectrum. For instance, a hard signal spectrum like E^{-2}

would suggest a tighter cut than a softer $E^{-2.5}$ spectrum. After imposing level 2 cuts the detector still has an effective area of $\sim$0.3 km^2 for upward-moving muons of a few tens of GeV. Additional cuts from level 2 on, optimized with respect to different signal hypotheses, in some cases shift the threshold considerably to higher energies. Fig. 5 includes the effective area after adding energy-separation cuts requiring the channel multiplicity N_{ch} to be larger than 20 and 30 respectively. Such cuts are applied in the search for high-energy neutrinos from steady point sources. The tighter requirement ($N_{ch} > 30$), for instance, is the result of an optimization procedure (see Section 5) assuming a pointlike E^{-2} signal and an exposure time of one year. This cut only affects events at energies below 10 TeV (where most of the atmospheric background lies), while full efficiency is retained at higher energies. For an $E^{-2.5}$ signal spectrum and the same exposure time, the optimization yields a looser cut, $N_{ch} > 20$, which has less impact on the energy threshold. (The impact on the energy threshold resulting from the additional N_{ch} cuts optimized for diffuse and pointlike E^{-2} signals can also be seen in Figs. 13 and 17. Note, however, that these figures show the energy spectra of the primary neutrino, rather than the muon energy at the detector.)

While in Fig. 5 the effective area was averaged over all directions throughout the northern sky, Fig. 6 shows the effective area as a function of zenith angle of the muon track over the full sky, from vertically upward-going ($\cos\Theta_\mu = -1$) to vertically downward-going ($\cos\Theta_\mu = 1$). In each of the four discrete energy intervals shown separately, the effective area reflects an average value for a sample of muons induced by neutrinos with an initial energy spectrum proportional to E^{-2}. The detector will have an effective detection area of one square kilometer for upward-moving muons in the TeV range. Above 100 TeV the selection allows the detection of downward neutrinos, i.e., an observation of the southern sky ($\cos\Theta_\mu > 0$). In the PeV range the effective area for downward muons is at least 0.6 km^2, increasing towards the horizon. This means that for these energies IceCube can observe a large part of our Galaxy, including the Galactic center. When seen from the South Pole, the Galactic center is located approximately 30° above the horizon, which corresponds to $\cos\Theta_\mu = 0.5$ in detector coordinates. In that direction, the effective area is $\sim$0.2 km^2 at 0.1–1 PeV, rising to 0.8 km^2 for PeV muons.

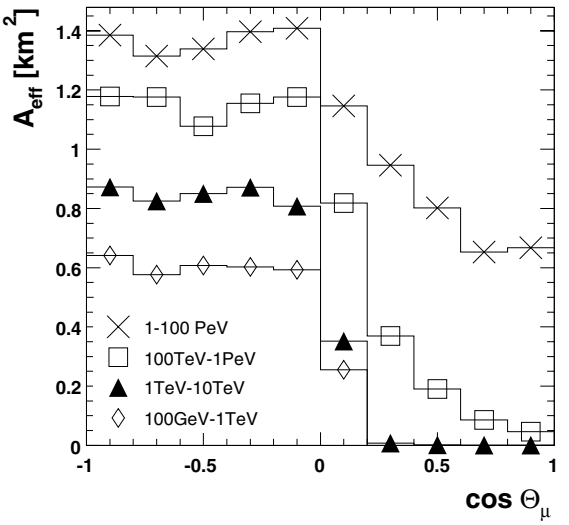

Fig. 6. *Effective area at level 2 as a function of the zenith angle.* The effective area was calculated for muons in four separate energy ranges after imposing level 2 cuts.

4.4. Angular resolution

The angular resolution for reconstructed muon tracks is an important quantity in the search for neutrinos from point sources. A higher angular resolution allows the use of a smaller search bin, resulting in a lower background rate per bin and thus a higher signal-to-noise ratio.

We characterize the reconstruction error by the angle Ψ between the true and the reconstructed directions of the simulated muon tracks. Fig. 7 shows the distribution of Ψ at level 2 for the entire signal sample of muons from neutrinos with an E^{-2} energy spectrum. The median of this distribution can be used as a simple measure of the pointing resolution. It corresponds to the size (i.e., the opening half-angle) of the angular cone about the true track direction in which 50% of the reconstructed tracks lie. The overall median angular error for the E^{-2} signal sample is about 0.8°.

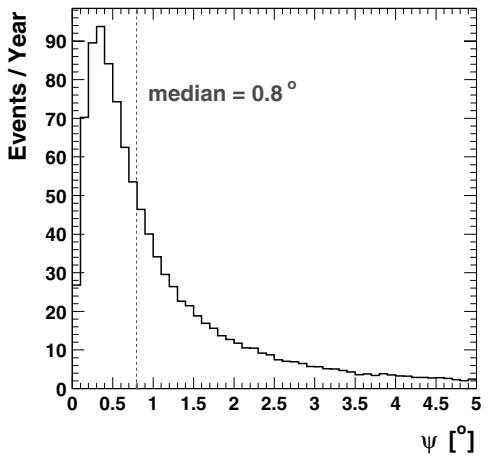

Fig. 7. *Angular reconstruction error for neutrino-induced muon events.* The angle Ψ between the reconstructed and the true direction of the muon track was calculated for a sample of neutrino-induced muons, for a primary neutrino energy spectrum proportional to E^{-2}, and is shown here after level 2 selection.

However, the reconstruction accuracy depends on the energy and angle of incidence of the muon. The median angular error is shown in Fig. 8 as a function of the cosine of the zenith angle of the muon for four different muon energy ranges.

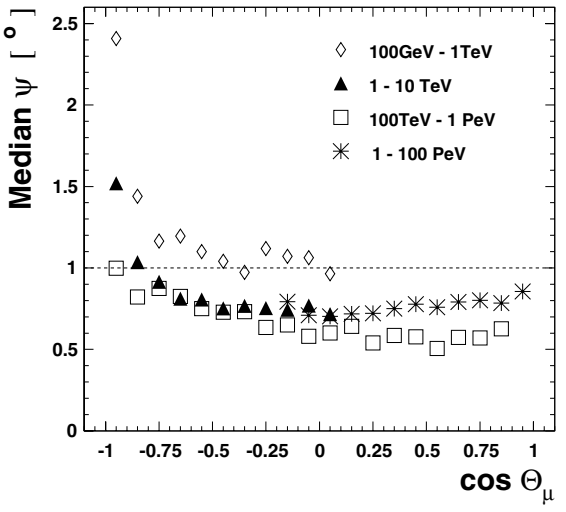

Fig. 8. *Pointing resolution for neutrino-induced muon events.* The median space-angle error of the LR is shown as a function of the zenith angle of the incident muon. The resolution was calculated for an energy spectrum proportional to E^{-2} and after applying level 2 cuts.

For muon energies from 100 GeV to 1 TeV the median angular error approaches 1° for tracks with zenith angles smaller than roughly 140° ($\cos\Theta_\mu > -0.8$). For nearly vertical, upward-going tracks of low-energy muons the angular resolution is worse, because such events are likely to cause hits in optical modules on a single string only. However, the reconstruction accuracy in this energy range is similar to the mean angle between the muon and the initial neutrino. In the more promising higher energy range, a few TeV and above, the resolution is substantially higher and its zenith-angle dependency weaker. Most of the signal in the TeV–PeV range will be reconstructed with an accuracy significantly better than 1°. The angular error for muons with energies between 1 and 100 PeV is shown only above $\cos\Theta_\mu > -0.15$, i.e., only down to 10° or so below the horizon, since the Earth becomes opaque to muon neutrinos with sufficient energy to induce muons at these energies. For downward muons, the reconstruction error is smaller for sub-PeV muons than for muons in the PeV range. This is due to the angular selection at level 2 (cut 4 in Table 1) which only retains events with zenith angles less than 85° if they have a large channel multiplicity N_{ch}. Muons with TeV energies, compared to the much brighter PeV muons, have to travel a longer path inside the instrumented volume in order to fulfill the N_{ch} requirement, and will thus be reconstructed more accurately. A significant improvement in the reconstruction of PeV events is expected with further development of the reconstruction, in particular from including amplitude and waveform information.

Apart from using the median angular error, the reconstruction resolution can also be characterized in terms of the width of the two-dimensional distribution of the angular deviation of reconstructed track directions from the true track direction. This so-called "point-spread function," expressed in spherical detector coordinates Θ and Φ such that all bins span equal solid angles, is shown in Fig. 9.

This two-dimensional function being fairly symmetric, we calculate the density of reconstructed tracks (number of tracks per steradian) as

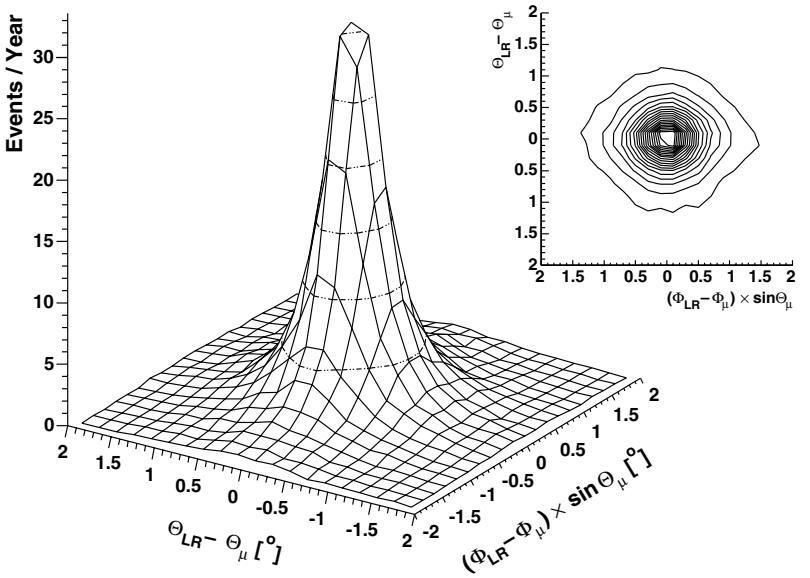

Fig. 9. *Point-spread function in detector coordinates.* The full Monte Carlo event sample of neutrino-induced muons weighted to an E^{-2} energy spectrum of the initial neutrinos was used after applying level 2 cuts.

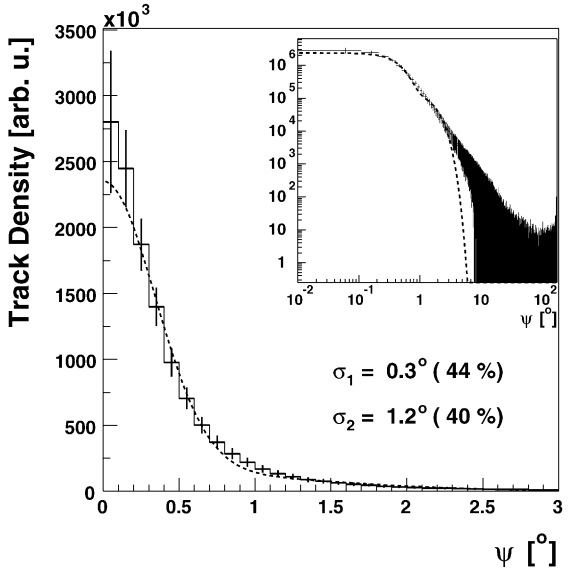

Fig. 10. *One-dimensional point-spread function.* The density distribution, after level 2 selection, of reconstructed tracks about the true muon direction as a function of the angle Ψ between reconstructed and true track was fitted with the sum of two Gaussians.

a function of the space angle Ψ from the true track by normalizing each bin in the space-angle distribution (Fig. 7) with the corresponding solid-angle element. The resulting one-dimensional point-spread function is shown in Fig. 10. This density distribution is not described well by a single Gaussian, but can be fitted reasonably well with a sum of two Gaussians. Such a fit yields standard deviations of $\sigma_1 = 0.3°$ and $\sigma_2 = 1.2°$ for the two Gaussians. Integrating the fitted density functions over the full solid angle shows that the narrower Gaussian accounts for about 44% of the event statistics, the broader Gaussian accounts for 40%, and roughly 16% of the events lie in the tail of the distribution where the track density is not described by a double Gaussian.

5. Sensitivity to astrophysical sources of muon neutrinos

In most theoretical models, the production of high-energy cosmic rays is accompanied by the production of mesons. Prominent candidates for cosmic-ray sources are putative cosmic accelerators like AGN, microquasars, supernova remnants and GRBs. Theoretical models for such objects usually involve shock acceleration of protons. The

protons interact with ambient matter or radiation fields producing mesons that subsequently decay into neutrinos. The spectral distribution of neutrinos expected from cosmic accelerators is $dN_\nu/dE_\nu \propto E_\nu^{-2}$, or even harder, depending on the predominant meson-production mechanism in the source and on full particulars of the acceleration.

The sum of all cosmic accelerators in the universe should produce an isotropic flux of high-energy neutrinos, which would be observable as an excess above the diffuse flux of atmospheric neutrinos. The absolute fluxes from individual sources may be small, and require careful selection in order to be resolved. However, in this case, background can be strongly suppressed since the number of background events will be reduced with the size of the spatial search bin or—in case of transient phenomena—the duration of the observation time window.

In the following we calculate the sensitivity for diffuse fluxes of cosmic muon neutrinos as well as for fluxes from individual point sources, both steady and transient (GRBs). In contrast to former analyses, which were based on simple assumptions on the detector effective area as well as on its energy resolution [21–23], the method we apply involves exclusively event observables that will be available from real data taken by IceCube.

5.1. Calculation of the sensitivity

We explore the sensitivity of the IceCube detector to cosmic neutrino fluxes in two ways. First we consider the limits that would be placed on models of neutrino production if no events were to be seen above those expected from atmospheric neutrinos. Second, we evaluate the level of source flux required to observe an excess at a given significance level.

5.1.1. Limit setting potential

Feldman and Cousins have proposed a method to quantify the "sensitivity" of an experiment independently of experimental data by calculating the average upper limit, $\bar{\mu}$, that would be obtained in absence of a signal [45]. It is calculated from the mean number of expected background events, $\langle n_b \rangle$, by averaging over all limits obtained from all possible experimental outcomes. The average upper limit is the maximum number of events that can be excluded at a given confidence level. That is, the experiment can be expected to constrain any hypothetical signal that predicts at least $\langle n_s \rangle = \bar{\mu}$ signal events.

From the 90% c.l. average upper limit, we define the "model rejection factor" (*mrf*) for an arbitrary source spectrum Φ_s predicting $\langle n_s \rangle$ signal events, as the ratio of the average upper limit to the expected signal [23]. The average flux limit Φ_{90} is found by scaling the normalization of the flux model Φ_s such that the number of expected events equals the average upper limit

$$\Phi_{90} = \Phi_s \times \frac{\bar{\mu}_{90}}{\langle n_s \rangle} \equiv \Phi_s \times mrf. \tag{2}$$

5.1.2. Discovery potential

For our purposes, a phenomenon is considered "discovered" when a measurement yields an excess of 5σ over background, meaning that the probability of the observation being due to an upward fluctuation of background is less than 2.85×10^{-7}, this number being the integral of the one-sided tail beyond 5σ of a normalized Gaussian. From the background expectation $\langle n_b \rangle$, we can determine the minimum number of events n_0 to be observed to produce the required significance as

$$\sum_{n_{obs}=n_0}^{\infty} P(n_{obs}|\langle n_b \rangle) \leqslant 2.85 \times 10^{-7}, \tag{3}$$

where $P(n_{obs}|\langle n_b \rangle)$ is the Poisson probability for observing n_{obs} background events. The minimum detectable flux $\Phi_{5\sigma}$ for any source model can then be found by scaling the model flux Φ_s such that $\langle n_s \rangle + \langle n_b \rangle = n_0$.

If a real signal source of average strength $\Phi_{5\sigma}$ is present, the probability of the combination of signal and background producing an observation sufficient to give the required significance (i.e., an observation of n_0 events or greater) is

$$P_{5\sigma} = \sum_{n_{obs}=n_0}^{\infty} P(n_{obs}|\langle n_s \rangle + \langle n_b \rangle). \tag{4}$$

Thus we cannot say that an underlying signal strength will always produce an observation with

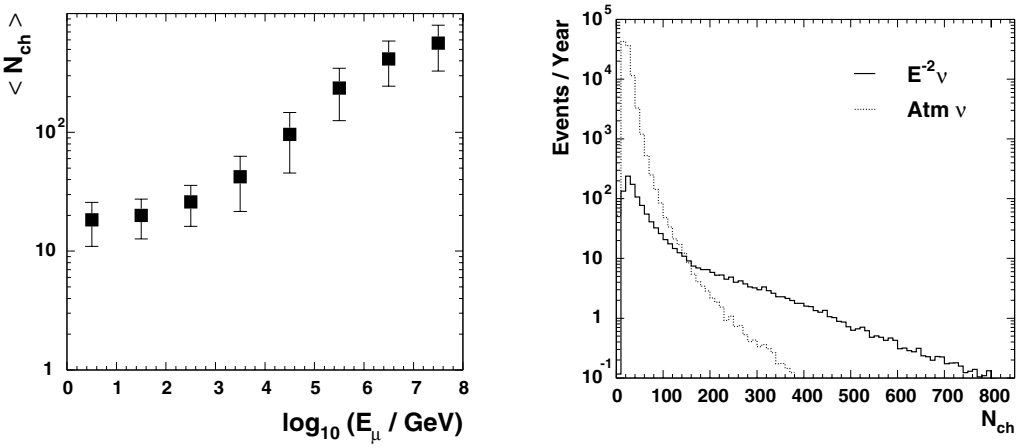

Fig. 11. *Channel multiplicity.* Left: Correlation between muon energy at closest approach to the detector center and detected channel multiplicity. The filled squares show the mean number of OMs with at least one recorded hit, averaged over one decade in energy. The vertical bars indicate the spreads of the corresponding $N_{\rm ch}$ distributions. Right: Detected channel multiplicity for E^{-2} signal and atmospheric background. The signal event rate is normalized to a flux of $E_\nu^2 \times {\rm d}N_\nu/{\rm d}E_\nu = 10^{-7}\ {\rm cm}^{-2}\,{\rm s}^{-1}\,{\rm sr}^{-1}\,{\rm GeV}$.

5σ significance, but we can find the signal strength such that the probability of $P_{5\sigma}$ is close to certainty, e.g., 70%, 90% or 99%.

5.2. Diffuse flux sensitivity

Many models have been developed that predict a diffuse neutrino flux to be expected from the sum of all active galaxies in the universe. First we will consider the potential of IceCube to both place a limit on, and detect, a generic diffuse flux following an E^{-2} spectrum. After looking in detail at this case we summarize the capabilities of the detector to place limits on a few models with spectral shapes different from E^{-2}.

We use the simplest observable related to muon energy, the multiplicity $N_{\rm ch}$ of hit channels per event, for an energy-discrimination cut, in order to reject the steep spectrum of events induced by atmospheric neutrinos and retain events from the harder extraterrestrial diffuse spectrum. [3] The correlation between muon energy at closest approach to the detector center and channel multiplicity is shown in the left plot of Fig. 11. The right plot compares the $N_{\rm ch}$ distributions for an E^{-2} signal and atmospheric-neutrino background.

We determine the $N_{\rm ch}$ cut (rejecting events below the cut-off) that maximizes the sensitivity by optimizing the cut with respect to the model rejection factor (*mrf*) [23]. For each possible cut value we compute the *mrf* from the number of remaining signal and background events. The cut is then applied where the *mrf* is minimized.

This procedure is illustrated in Fig. 12. The left plot shows the average number of signal and background events, together with the average upper limit $\bar{\mu}_{90}$, expected from one year's exposure to a simulated cosmic-neutrino flux of $E_\nu^2 \times {\rm d}N_\nu/{\rm d}E_\nu = 10^{-7}\ {\rm cm}^{-2}\,{\rm s}^{-1}\,{\rm sr}^{-1}\,{\rm GeV}$ as a function of a cut in $N_{\rm ch}$. The corresponding *mrf*, shown in the right plot, reaches its minimum of 8.1×10^{-2} for $N_{\rm ch} > 227$, which translates to an overall flux limit of $E_\nu^2 \times {\rm d}N_\nu/{\rm d}E_\nu = 8.1 \times 10^{-9}\ {\rm cm}^{-2}\,{\rm s}^{-1}\,{\rm sr}^{-1}\,{\rm GeV}$. This limit applies to the flux of extraterrestrial muon neutrinos measured at the Earth. In the presence of neutrino oscillations, the constraint on the flux escaping cosmic sources must be modified accordingly. For maximal mixing [46,47] between muon- and tau-neutrinos during propagation to the Earth, one would expect the flux of muon neutrinos at the Earth to be half the flux at the

[3] An improved energy separation is expected from the use of a more sophisticated energy reconstruction using individual hit amplitude and/or the full waveform information.

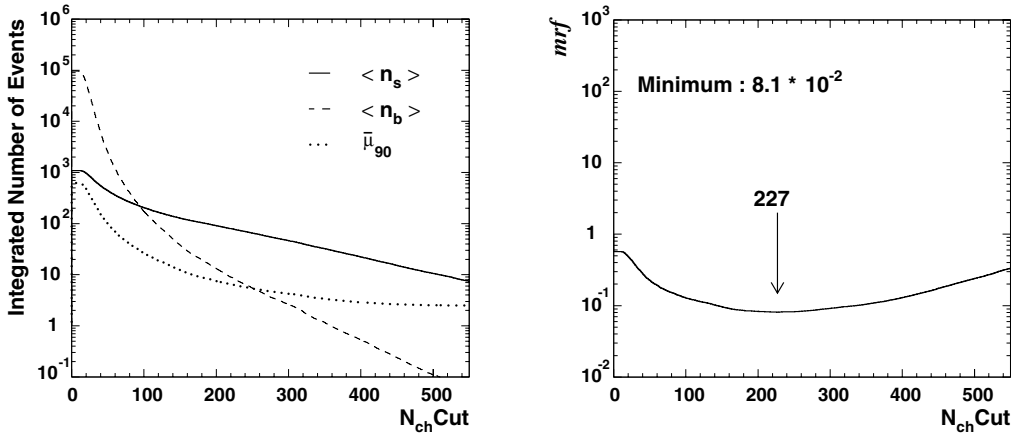

Fig. 12. *Optimization of channel multiplicity cut.* Left: Mean number of expected signal (solid) and background (dashed) events in one year for a model source flux of $E_\nu^2 \times dN_\nu/dE_\nu = 10^{-7}$ cm^{-2} s^{-1} sr^{-1} GeV, and the corresponding 90% c.l. average upper limit (dotted), as a function of a cut in channel multiplicity. Right: The model rejection factor calculated from the left plot has a minimum for $N_{ch} > 227$.

source. The limit on the muon-neutrino flux *produced* in cosmic sources would thus be a factor of two higher. Here, "cosmic neutrino flux" refers to the flux of muon neutrinos measured at the Earth.

In the above simulation, in one year 75 signal events on average are predicted to pass the optimized N_{ch} cut, compared to eight background events from atmospheric neutrinos. The background expectation was calculated using the `rqpm` model for the prompt-charm contribution, according to which prompt charm decays account for 80% of the remaining atmospheric neutrinos. Using the corresponding prediction based on the `TIG` model would result in an improvement of the average flux limit by roughly a factor of 2.

The energy spectra of the incident signal and background neutrinos are shown in Fig. 13. The final N_{ch} cut translates into a detection threshold of about 100 TeV. This threshold results from the optimization to one particular signal hypothesis,

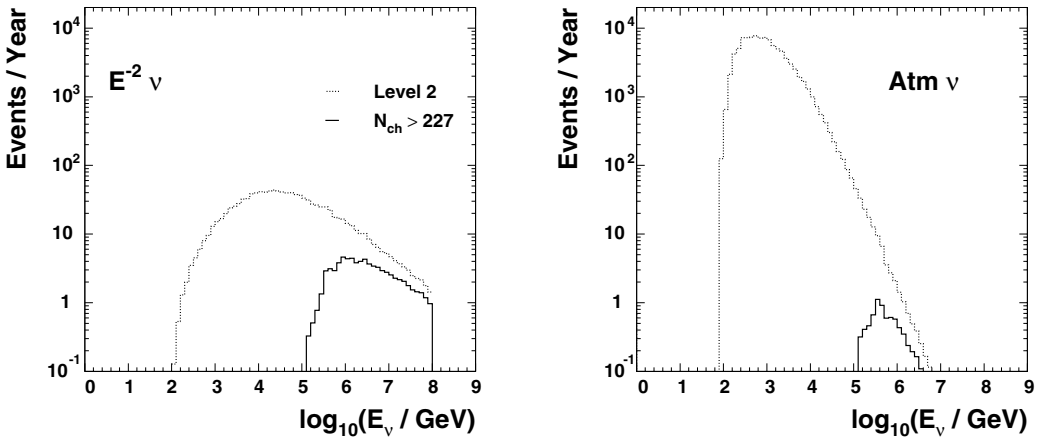

Fig. 13. *Energy spectra of selected neutrinos* for a diffuse signal flux of $E_\nu^2 \times dN_\nu/dE_\nu = 10^{-7}$ cm^{-2} s^{-1} sr^{-1} GeV (left) and for atmospheric neutrinos (right), after level 2 cuts (dotted lines) and after application of the optimized $N_{ch} > 227$ cut (solid lines). The cut-off in the signal spectrum at 10^8 GeV is due to the limited energy range in the simulation.

an E^{-2} neutrino spectrum extending up to energies of 10^8 GeV, where it has an artifical cut-off (the simulation ends). Extrapolating the signal spectrum beyond the cut-off leads to the conclusion that for an E^{-2} source a few percent of the final signal sample would lie at energies above 100 PeV, provided the flux of neutrinos extends to such high energies. Without the cut-off in the energy spectrum of our simulated event sample, the calculated sensitivity would be improved at the same scale as the signal event rate is increased, i.e., the average upper limit after one year of operation is overestimated by a few percent. The effect is stronger for longer exposure times and for harder spectra, since the optimal energy-separation cut will be tighter, shifting the energy threshold towards higher energies and thereby increasing the fraction of events with energies above the cut-off.

The sensitivity attained after one year of data taking is already well below the diffuse bound calculated by Waxman and Bahcall [48]. (Their limit holds for optically thin cosmic-ray sources, under the assumption that these sources produce the observed flux of high-energy cosmic rays.) A flux at the level $E_\nu^2 \times \mathrm{d}N_\nu/\mathrm{d}E_\nu = 2.6 \times 10^{-8}$ $\mathrm{cm}^{-2}\,\mathrm{s}^{-1}\,\mathrm{sr}^{-1}\,\mathrm{GeV}$ is needed on average for a 5σ detection after a period of one year. This flux is forty times below the present best established 90% c.l. upper limit [9].

The improvement with time of the exclusion and discovery potential of the IceCube detector is summarized in Table 3. As the exposure time increases, the optimal multiplicity cut becomes tighter (i.e., higher), resulting in a better separation of signal and background. After data is taken over five years instead of one, the sensitivity is improved by a factor of about 2.5. The 5σ detection level given in Table 3 corresponds to the flux for which the average event rate from signal plus background exceeds the 5σ threshold. The signal strength at which the 5σ excess is produced at a fixed probability, is shown in Fig. 14 as a function of time. A signal of $E_\nu^2 \times \mathrm{d}E_\nu/\mathrm{d}N_\nu = 10^{-8}$ $\mathrm{cm}^{-2}\,\mathrm{s}^{-1}\,\mathrm{sr}^{-1}\,\mathrm{GeV}$, for instance, would be detected with a probability of 70% after five years of data taking.

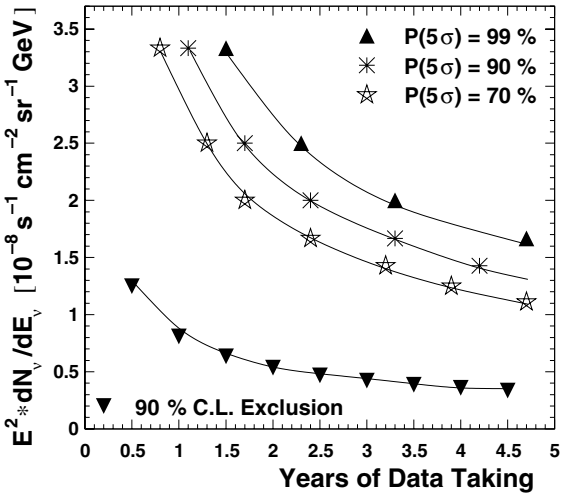

Fig. 14. *Sensitivity to diffuse neutrino fluxes.* Improvement with time of the diffuse flux with an E^{-2} spectrum that can be excluded at 90% c.l. (lower curve) or detected at a 5σ level with a fixed probability $P(5\sigma)$ (upper curves).

Apart from the generic case of an E^{-2} spectrum, which is typical for scenarios that involve meson production in interactions of shock-accelerated cosmic rays with matter, we have varied the signal slope towards flatter spectra. Such spectra would be expected from environments where cosmic rays predominantly interact on photon fields, e.g., AGN jets. For each alternative energy spectrum, we minimized the model rejection factor to find the N_{ch} cut for which the best sensitivity is attained. From

Table 3
Sensitivity to diffuse neutrino fluxes

Years	N_{ch} cut	$\langle n_{\mathrm{s}} \rangle$	$\langle n_{\mathrm{b}} \rangle$	$\bar{\mu}_{90}$	$E^2 \frac{\mathrm{d}N}{\mathrm{d}E}$ (90% c.l.)	$E^2 \frac{\mathrm{d}N}{\mathrm{d}E}(5\sigma)$
1	227	75.4	8.0	6.1	8.1×10^{-9}	2.6×10^{-8}
3	244	204.8	18.4	8.7	4.2×10^{-9}	1.2×10^{-8}
5	276	272.5	18.0	8.6	3.2×10^{-9}	9.9×10^{-9}

Expected limits, $E^2 \frac{\mathrm{d}N}{\mathrm{d}E}$ (90% c.l.), and minimal detectable fluxes, $E^2 \frac{\mathrm{d}N}{\mathrm{d}E}(5\sigma)$, in units of $\mathrm{cm}^{-2}\,\mathrm{s}^{-1}\,\mathrm{sr}^{-1}\,\mathrm{GeV}$ for a generic E^{-2} source spectrum. Event numbers correspond to a hypothetical source strength of $E_\nu^2 \times \mathrm{d}N_\nu/\mathrm{d}E_\nu = 10^{-7}$ $\mathrm{cm}^{-2}\,\mathrm{s}^{-1}\,\mathrm{sr}^{-1}\,\mathrm{GeV}$.

the number of background events remaining after imposing this cut, we determined the event average upper limit $\bar{\mu}_{90}$. As above, the simulated spectrum was then normalized such that the expected number of signal events equaled $\bar{\mu}_{90}$. The resulting normalization constant is a measure of the detector's sensitivity to signal of this specific spectral shape. The results obtained for source spectra proportional to E^{-1} and $E^{-1.5}$ are given in Table 4. The N_{ch} cut was optimized after normalizing the event samples to a data-taking period of three years. A signal with a harder energy spectrum allows a tighter N_{ch} cut and hence the optimization results in a lower average upper limit. For an E^{-1} source model, the maximum flux which is expected to be excluded at 90% c.l. after three years of operation is $\mathrm{d}N_\nu/\mathrm{d}E_\nu = 3.1 \times 10^{-16}\ (\mathrm{E/GeV})^{-1}\,\mathrm{cm}^{-2}\,\mathrm{s}^{-1}\,\mathrm{sr}^{-1}$. This limit is compared to the limit for an E^{-2} source spectrum in Fig. 15. The limit that can be placed on an $E^{-1.5}$ signal hypothesis is $\mathrm{d}N_\nu/\mathrm{d}E_\nu = 1.5 \times 10^{-12}$

Table 4
Sensitivity to diffuse neutrino fluxes for alternative source spectra

Source model	N_{ch} cut	$\bar{\mu}_{90}$	Expected 90% c.l. limit
$\mathrm{d}N_\nu/\mathrm{d}E_\nu \propto E^{-1}$	427	3.3	$3.1\times10^{-16}\ (\mathrm{E/GeV})^{-1}\,\mathrm{cm}^{-2}\,\mathrm{s}^{-1}\,\mathrm{sr}^{-1}$
$\mathrm{d}N_\nu/\mathrm{d}E_\nu \propto E^{-1.5}$	336	4.9	$1.5\times10^{-12}\ (\mathrm{E/GeV})^{-1.5}\,\mathrm{cm}^{-2}\,\mathrm{s}^{-1}\,\mathrm{sr}^{-1}$
MPR [49]	324	5.2	$\Phi_{\mathrm{MPR}} \times 1.9 \times 10^{-2}$
S&S [50]	250	8.3	$\Phi_{\mathrm{S\&S}} \times 2.3 \times 10^{-3}$

For each energy spectrum, the quoted expected limit is the maximum flux level which is expected to be excluded at 90% c.l. after three years of data taking. The flux predictions by MPR, Φ_{MPR}, and by Stecker and Salamon, $\Phi_{\mathrm{S\&S}}$, are still excludable when scaled down by factors 1.9×10^{-2} and 2.3×10^{-3} (the corresponding model rejection factors after N_{ch} cut optimization), respectively.

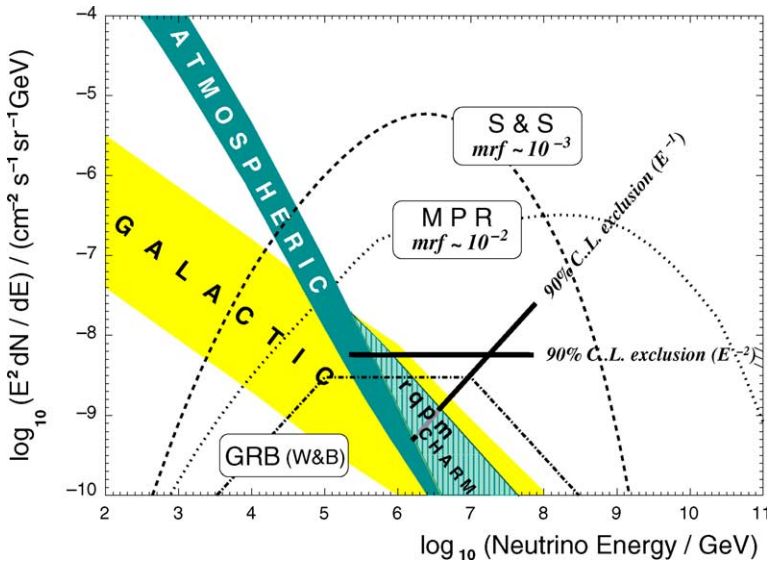

Fig. 15. *Expected sensitivity of the IceCube detector to diffuse neutrino fluxes.* Solid lines indicate the 90% c.l. limit for various differential signal energy spectra, calculated for a data-taking period of three years. The lines extend over the energy range containing 90% of the expected signal. The dashed curve indicates the expected diffuse neutrino flux according to the Stecker and Salamon model for photo-hadronic interactions in AGN cores [50]. The model rejection factor after three years of data taking for this signal shape is 2.3×10^{-3}. The dotted curve corresponds to the MPR upper bound on neutrino emission from photo-hadronic interactions in AGN jets [49]. The model rejection factor for this model is 1.9×10^{-2} after three years of data taking. Also shown is the prediction from the GRB model by Waxman and Bahcall [48] (dash-dotted line).

$(E/GeV)^{-1.5}\,cm^{-2}\,s^{-1}\,sr^{-1}$ after three years of operation.

Mannheim, Protheroe and Rachen (MPR) [49] have calculated a theoretical upper bound on the diffuse neutrino flux arising from photo-hadronic interactions in unresolved AGN jets in the universe. Their flux bound is shown in Fig. 15 (labeled MPR). In order to compare this bound to the IceCube sensitivity we have computed the model rejection factor for a hypothetical diffuse signal with an energy spectrum following this upper bound. However, since the MPR model extends to energies well beyond 100 PeV (the artificial cut-off in the simulation), the simulated signal will not include events predicted at the highest energies. The model rejection factor for the MPR model ($E_\nu < 100$ PeV) is 1.9×10^{-2} after three years of data taking, meaning that after this period IceCube will be sensitive to fluxes of similar spectral shape, but fifty times lower than the MPR bound.

Finally, we have selected one particular model by Stecker and Salamon [50] for neutrinos from proton interactions on the UV thermal photon field in AGN cores. The corresponding diffuse flux prediction is labeled S&S in Fig. 15. The model rejection factor corresponding to three years of data taking is in this case 2.3×10^{-3}.

5.3. Sensitivity to point sources

An excess of events from a particular direction in the sky suggests the existence of a point source. The ability of the detector to reconstruct muon tracks to within 1° of their true direction allows a search window to be used with a size that greatly reduces the background, while retaining a large fraction of the signal. This allows a loosening of the energy-separation cut.

We restrict this analysis to the case of a point-source search for candidate sources in the northern sky. That is, we do not simulate a cluster or grid search, but instead consider the case where an angular search bin is fixed by the direction of the candidate source under scrutiny. In reality the sensitivity will depend on the declination of the source location. For simplicity of presentation we calculate averaged event rates for all declinations throughout the northern sky.

We use an angular search cone with a 1° opening half-angle centered about the direction of a hypothetical point source (i.e., we allow an angular deviation of 1° in any direction). After application of the standard cut selection (level 2), we again optimize the N_{ch} cut with respect to the model rejection potential for a point source following an E^{-2} spectrum. A cut at a channel multiplicity of $N_{ch} = 30$, combined with the angle cut of one degree, leads to the best average flux upper limit of $E_\nu^2 \times dN_\nu/dE_\nu = 5.5 \times 10^{-9}\ cm^{-2}\,s^{-1}\,GeV$ after one year of data taking. A flux three times greater will on average produce a 5σ signal.

Table 5 and Fig. 16 summarize the improvement of the limit with increased exposure time. After three years of operation IceCube can be expected to place flux limits on potential sources at a level of $E_\nu^2 \times dN_\nu/dE_\nu \sim 2.4 \times 10^{-9}\ cm^{-2}\,s^{-1}\,GeV$, while the discovery probability for a flux three times stronger is higher than 70%. After five years of operation a source emitting a flux of $E_\nu^2 \times dN_\nu/dE_\nu \sim 6 \times 10^{-9}\ cm^{-2}\,s^{-1}\,GeV$ would be observed at 5σ significance with a probability of 70%.

As in the case of a diffuse signal, we have varied the energy spectrum for the signal hypothesis in order to see how it affects the sensitivity to point sources. The results listed in Table 6 correspond to three years of data taking.

Table 5
Sensitivity to neutrino point sources

Years	N_{ch} cut	$\langle n_s \rangle$	$\langle n_b \rangle$	$\bar{\mu}_{90}$	$E^2\frac{dN}{dE}$ (90% c.l.)	$E^2\frac{dN}{dE}(5\sigma)$
1	30	62.8	1.4	3.6	5.5×10^{-9}	1.7×10^{-8}
3	40	142.3	1.3	3.5	2.4×10^{-9}	7.2×10^{-9}
5	42	213.7	1.4	3.6	1.7×10^{-9}	4.9×10^{-9}

Expected limits, $E^2\frac{dN}{dE}$(90%c.l.), and minimal detectable fluxes, $E^2\frac{dN}{dE}(5\sigma)$, in units of $cm^{-2}\,s^{-1}$ GeV for a generic E^{-2} source spectrum and different exposure times. Signal event rates correspond to a hypothetical source strength of $E_\nu^2 \times dN_\nu/dE_\nu = 10^{-7}\ cm^{-2}\,s^{-1}\,GeV$. Background event rates include `rqpm` charm neutrinos.

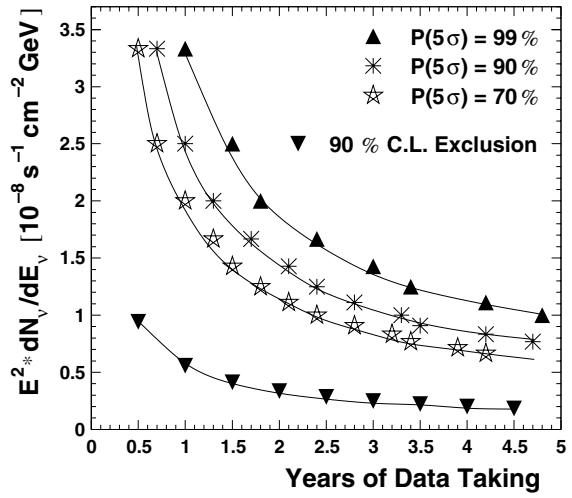

Fig. 16. *Sensitivity to pointlike neutrino emission.* Improvement with time of the point-source flux with an E^{-2} source spectrum that can be excluded at 90% c.l. (lower curve) or detected at a 5σ level with a fixed probability $P(5\sigma)$ (upper curves).

Fig. 17 shows the energy spectra of both the remaining signal events and the remaining events from the atmospheric-neutrino background after applying standard level 2 cuts and after cutting at $N_{ch} > 30$. This selection results in an effective energy threshold of about 1 TeV. Since most of the signal in this case is in the TeV–PeV range, the energy cut-off at 10^8 GeV in the simulation has a negligible impact on the result. The shown results are valid for the `rqpm` prediction for prompt neutrinos. Using the `TIG` model improves the sensitivity by about 2%.

5.4. Gamma ray burst sensitivity

Although the progenitors of GRBs are unknown, observations indicate the existence of a fireball. The coexistence of nucleons and photons

Table 6
Sensitivity to point-source fluxes for various source energy spectra

Source model	N_{ch} cut	$\bar{\mu}_{90}$	Expected 90% c.l. limit
$dN_\nu/dE_\nu \propto E^{-1}$	58	2.7	2.4×10^{-15} (E/GeV)$^{-1}$ cm^{-2} s^{-1}
$dN_\nu/dE_\nu \propto E^{-1.5}$	49	2.9	4.5×10^{-12} (E/GeV)$^{-1.5}$ cm^{-2} s^{-1}
$dN_\nu/dE_\nu \propto E^{-2}$	40	3.5	2.4×10^{-9} (E/GeV)$^{-2}$ cm^{-2} s^{-1}
$dN_\nu/dE_\nu \propto E^{-2.5}$	24	6.1	3.8×10^{-5} (E/GeV)$^{-2.5}$ cm^{-2} s^{-1}

For each energy spectrum, the quoted expected limit is the maximum flux level which is expected to be excluded at 90% c.l. after three years of data taking.

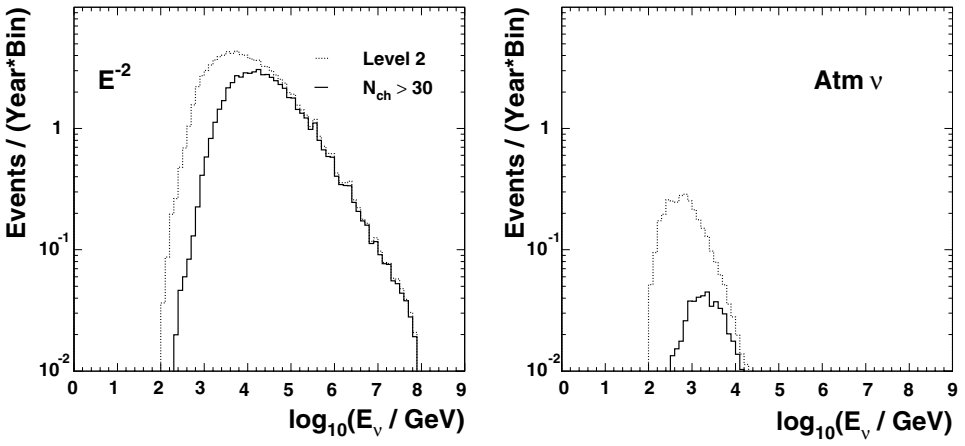

Fig. 17. *Energy spectra of selected neutrinos* for a point-source signal with an assumed flux of $E_\nu^2 \times dN_\nu/dE_\nu = 10^{-7}$ cm^{-2} s^{-1} GeV (left) and for atmospheric neutrinos including `rqpm` charm (right). The selection corresponds to level 2 cuts (dotted lines) and additional application of the optimized cut $N_{ch} > 30$ (solid lines). The spatial search bin was defined by an angular cone with a 1° opening half-angle.

in the fireball may result in the production of neutrinos.

Waxman and Bahcall [48] calculated the expected flux of neutrinos from the sum of all GRBs by assuming that they are the source of the observed flux of cosmic rays. The Waxman–Bahcall model results in a broken power-law neutrino spectrum given by

$$\Phi_{\mathrm{W\&B}} = \frac{\mathrm{d}N_\nu}{\mathrm{d}E_\nu} = \begin{cases} \dfrac{A}{E_\nu E_\nu^{\mathrm{b1}}}, & E_\nu < E_\nu^{\mathrm{b1}} \\ \dfrac{A}{E_\nu^2}, & E_\nu^{\mathrm{b1}} < E_\nu < E_\nu^{\mathrm{b2}}, \end{cases} \quad (5)$$

where the break energy E_ν^{b1} lies at $\sim 10^5$ GeV. Above $E_\nu^{\mathrm{b2}} = 10^7$ GeV the spectrum steepens again by one power in energy. With a full-sky GRB rate of $\sim$1000 per year, as assumed by Waxman and Bahcall, the normalization constant in Eq. (5) would amount to $A \sim 3 \times 10^{-9}$ cm^{-2} s^{-1} sr^{-1} GeV. [4] This neutrino flux is shown in Fig. 15 (labeled GRB). It appears to be below the diffuse-flux sensitivity level of IceCube. However, the search for neutrinos accompanying GRBs is essentially background-free, due to the requirement that the neutrino events are coincident in both direction *and* time with satellite observations of the gamma rays.

The search for neutrinos from GRB sources involves summing over the observation time and spatial search windows for many separate bursts. For this analysis we have used a hypothetical observation duration of 10 s and a spatial search cone of 10° (opening half-angle) centered about the direction of each GRB. We have only considered events in the northern sky, where the search is not limited by downward cosmic-ray-muon background. From 500 bursts in 2π sr (out of the 1000 assumed over the full sky in one year) we would expect 13 neutrino-induced upward muons per year after applying standard level 2 quality cuts. The background of atmospheric neutrinos is strongly reduced by the spatial and temporal coincidence requirements. With almost full retention of the signal ($\langle n_s \rangle = 12.3$ after imposing the coincidence requirements), the atmospheric neutrino background expectation is reduced to roughly 0.1 event. This low background expectation allows the exclusion of signals of mean intensity $\bar{\mu}_{90} = 2.5$ events per year at 90% classical confidence, which translates into a model rejection factor of $mrf = 0.2$, meaning that the experiment will be sensitive to a neutrino flux with roughly one fifth of the intensity originally calculated by Waxman and Bahcall (Table 7). This, in turn, means that a sample of 100 observed bursts would suffice to exclude the Waxman and Bahcall model. A 5σ detection would require the observation of $n_0 = 5$ neutrino events, which corresponds to the mean number of events expected from 203 bursts. In this case the probability to actually observe a 5σ excess is about 58%. With 500 bursts this probability climbs to 99%.

The time period after which we can expect a detection depends on the efficiency of gamma-ray observations, since the search strategy requires the GRBs to trigger satellite-borne detectors. Assuming that future gamma-ray observations will provide a few hundred triggered bursts per year, we can conclude that IceCube has excellent prospects to reveal the neutrino signal possibly emerging from gamma-ray bursters within a very short time. The analysis of data taken over one year would presumably suffice to yield a 5σ signal, provided the model by Waxman and Bahcall predicts neutrino fluxes at the right scale. Moreover, the sensitivity given above is obtained when employing the most conservative search strategy, namely searching only one hemisphere for the signal of upward neutrinos. However, the drastic background reduction that follows from restricting the search to a short time window about each observed GRB's detection time will result in a sizable acceptance also for signal from above the horizon.

5.5. Systematic uncertainties and possible improvements

The systematic uncertainty in the given flux limits is presently dominated by three components. The largest is an uncertainty in the angular dependence of the OM sensitivity, including the effect of the refrozen ice around the OM. A local

[4] A more recent calculation yielded a normalization constant which is about three times larger [51]. The event rates given here do not include this factor, since we have used the normalization originally calculated by Waxman and Bahcall in [48].

Table 7
Sensitivity to neutrino fluxes in coincidence with GRBs

GRBs	Time window	Angular cone	$\langle n_s \rangle$	$\langle n_b \rangle$	$\bar{\mu}_{90}$	Flux limit
500	10 s	10°	12.3	0.1	2.5	$0.2 \times \Phi_{W\&B}$

Average numbers of signal and background events expected for a sample of 500 observed GRBs, given a neutrino spectrum $dN_\nu/dE_\nu = \Phi_{W\&B}$ (as defined in Eq. (5)) and an intensity as calculated by Waxman and Bahcall in [48]. The event numbers are summed over all temporal and spatial search windows centered about each GRB. A neutrino flux following this energy spectrum is expected to be excludable by IceCube at an intensity 0.2 times the intensity originally calculated by Waxman and Bahcall.

increase in light scattering from air bubbles trapped in the vicinity of the OM translates into a modulation of its angle-dependent acceptance. This component is followed in size by uncertainties in the absolute OM sensitivity and uncertainties related to modeling and implementation of the optical properties of the bulk ice in the simulation. For the comparatively small AMANDA-B10 array the inclusion of all components of uncertainty weakens the point source flux limit by 25% compared to when the nominal simulation values are used [52]. The variation of some of these parameters in simulations of the larger AMANDA-II array and for IceCube indicates that for larger arrays the systematic uncertainties of the basic input parameters become less important, except for muon energies close to the detection threshold. For instance, increasing the absolute OM sensitivity in IceCube by a factor of two results in a 25% (10%) larger effective area at 1 (10) TeV. Taking into account that uncertainties in limits depend weaker-than-linearly on uncertainties in effective area [52], we estimate the overall uncertainties in the limits for E^{-2} signal derived above to be at most 20%.

However, a number of improvements of detector properties will reduce the systematic uncertainties and enhance the performance of IceCube compared to AMANDA. Using glass spheres and PMT glass with higher UV transparency or, alternatively, covering the glass spheres with wavelength-shifting film, will increase the OM sensitivity in the UV range and improve light collection. This will increase the overall sensitivity and angular resolution, particularly at *low energies*. Information extracted from the full PMT waveforms [5] will improve both angular resolution and energy reconstruction at *high energies*. Finally, the inclusion of information provided by the IceTop surface array will enhance the rejection power with respect to downward-moving atmospheric muons. This tool, unique to IceCube, is expected to be particularly helpful for rejecting events with coincident muons from independent air showers and would allow the loosening of other rejection criteria, thereby enhancing the signal efficiency.

[5] Waveform information will be available also in AMANDA data from 2003 onward.

6. Summary

We have described the expected performance of the IceCube detector in searching for muons from extraterrestrial neutrinos in the TeV–PeV energy range.

A Monte Carlo simulation of a realistic model detector was used to assess the sensitivity of the experiment. We simulated both neutrino-induced muons and muons produced from cosmic-ray interactions in the atmosphere with sufficient statistics to establish event-selection criteria and to infer expected event rates for each event class. The trigger rate due to downward muons produced in the atmosphere was found to be 1.7 kHz, including a 50 Hz rate due to uncorrelated air showers that produce time-coincident muons within the detector. Muons induced by atmospheric neutrinos are expected to cause about 0.8 million triggers per year. A benchmark flux of $E_\nu^2 \times dN_\nu/dE_\nu = 10^{-7}$ $cm^{-2}\,s^{-1}\,sr^{-1}\,GeV$ for the diffuse signal of astrophysical neutrinos results in 3300 triggers per year. Roughly one third of these events pass a set of standard quality cuts which at the same time reduces the background rate from misreconstructed downward-going muon tracks to the level of well-reconstructed upward-moving muons from atmospheric neutrinos.

In order to quantify the detector acceptance, we have computed the effective detector area for muons. After applying the standard quality criteria, the effective area exceeds one square kilometer for upward-moving muons with energies above 10 TeV. At this level of data reduction, 50% of all muons with these energies will be reconstructed with an accuracy of 0.8° or better. For energies above 100 TeV, the angular acceptance with respect to well-identified extraterrestrial neutrinos extends above the horizon and the effective area reaches 0.6 km^2 for near-vertical downward muons in the PeV range. This means that at high energies IceCube can observe a large part of the Galaxy, including the Galactic center.

In order to quantify the sensitivity to fluxes of astrophysical neutrinos, we have determined the flux normalization for a generic E^{-2} differential energy spectrum that corresponds to a detection with 5σ significance, or, in absence of signal, a 90% c.l. limit. We found a diffuse source strength of $E_\nu^2 \times dN_\nu/dE_\nu = 10^{-8}$ $cm^{-2}\,s^{-1}\,sr^{-1}$ GeV for the 5σ detection level and 4×10^{-9} $cm^{-2}\,s^{-1}\,sr^{-1}$ GeV for the exclusion potential of the detector, given an observation time of three years. This is two orders of magnitude below present experimental limits. For pointlike neutrino emission we found that, after three years, a flux of $E_\nu^2 \times dN_\nu/dE_\nu = 7 \times 10^{-9}$ $cm^{-2}\,s^{-1}$ GeV would result in a 5σ excess over background, while a flux of $E_\nu^2 \times dN_\nu/dE_\nu = 2 \times 10^{-9}$ $cm^{-2}\,s^{-1}$ GeV could be excluded at 90% c.l. Both numbers are averaged over all declinations throughout the northern sky. Integrated over all neutrino energies above 1 TeV, these fluxes translate to $F_\nu(E_\nu > 1\ \text{TeV}) = 7(2) \times 10^{-12}$ $cm^{-2}\,s^{-1}$.

We have also calculated the potential of IceCube to detect neutrinos in coincidence with GRB, following the model of Waxman and Bahcall. We found that a 5σ signal is expected from the observation of about 200 bursts, while an observation of 100 bursts would suffice to rule out the Waxman and Bahcall model.

Acknowledgements

This research was supported by the following agencies: National Science Foundation—Office of Polar Programs, National Science Foundation—Physics Division, University of Wisconsin Alumni Research Foundation, USA; Swedish Research Council, Swedish Polar Research Secretariat, Knut and Alice Wallenberg Foundation, Sweden; German Ministry for Education and Research, Deutsche Forschungsgemeinschaft (DFG), Germany; Fund for Scientific Research (FNRS-FWO), Flanders Institute to encourage scientific and technological research in industry (IWT), Belgian Federal Office for Scientific, Technical and Cultural affairs (OSTC), Belgium; Inamori Science Foundation, Japan; FPVI, Venezuela; The Netherlands Organization for Scientific Research (NWO).

References

[1] T.K. Gaisser, F. Halzen, T. Stanev, Phys. Rep. 258 (1995) 173.
[2] J.G. Learned, K. Mannheim, Ann. Rev. Nucl. Part. Sci. 50 (2000) 679.
[3] C. Spiering, Prog. Particle Nucl. Phys. 48 (2002) 43.
[4] P.K.F. Grieder et al., Nucl. Phys. Proc. Suppl. 43 (1995) 145.
[5] V.A. Balkanov et al., Nucl. Phys. Proc. Suppl. 75A (1999) 409.
[6] E. Andres et al., Astropart. Phys. 13 (2000) 1.
[7] J. Ahrens et al., Phys. Rev. D 66 (2002) 012005.
[8] I.A. Belolaptikov et al., Phys. Atom. Nucl. 63 (2000) 951.
[9] J. Ahrens et al., Phys. Rev. Lett. 90 (2003) 251101.
[10] T. Montaruli et al., in: Proceedings of the 26th ICRC, vol. 2, 1999, p. 213.
[11] E. Aslanides et al., A Deep Sea Telescope for High Energy Neutrinos, Proposal, 1999. Available from <astro-ph/9907432>.
[12] S. Bottai, in: Proceedings of the 26th ICRC, vol. 2, 1999, p. 456.
[13] G. Riccobene, in: Proceedings of the Workshop on Methodical Aspects of Underwater/Ice Neutrino Telescopes, DESY-PROC-2002-01, 2002, p. 61.
[14] J. Ahrens et al., The IceCube NSF Proposal, 2000.
[15] A. Biron et al., Participation of DESY-Zeuthen in the IceCube Project, Proposal to the DESY PRC, 2001.
[16] J. Ahrens et al., IceCube Conceptual Design Document, 2001.
[17] A. Goldschmidt, in: Proceedings of the 27th ICRC, vol. 3, 2001, p. 1237.
[18] M. Leuthold, in: Proceedings of the Workshop on Simulation and Analysis Methods for Large Neutrino Telescopes, DESY-PROC-1999-01, 1999, p. 484.
[19] H. Wissing, Diploma thesis, Humboldt Universität zu Berlin, 2001.

[20] X. Bai et al., in: Proceedings of the 27th ICRC, vol. 3, 2001, p. 981.
[21] I.F.M. Albuquerque, J. Lamoureux, G. Smoot. Available from <hep-ph/0109177>.
[22] J. Alvarez-Muniz, F. Halzen, Phys. Rev. D 63 (2001) 037302.
[23] G.C. Hill, K. Rawlins, Astropart. Phys. 19 (2003) 393.
[24] A.Bouchta et al., 2002. Available from <http://www.ifh.de/nuastro/software/siegmund/siegmund.html>.
[25] S.N. Boziev et al., INR-Preprint 0630, 1989.
[26] D. Heck, J. Knapp, Extensive Air Shower Simulation with CORSIKA: A User's Guide, Forschungszentrum Karlsruhe, Institut für Kernphysik, 2000.
[27] C.G.S. Costa, Astropart. Phys. 16 (2001) 193.
[28] T. Gaisser, M. Honda, Ann. Rev. Nucl. Part. Sci. 52 (2002) 153.
[29] G.C. Hill, Ph.D. thesis, University of Adelaide, 1996.
[30] A.D. Martin, W.J. Stirling, R.G. Roberts, Phys. Lett. B 354 (1995) 155.
[31] A.M. Dziewonski, D.L. Anderson, Phys. Earth Planet. Interiors 25 (1981) 297.
[32] P. Lipari, T. Stanev, Phys. Rev. D 44 (1991) 3543.
[33] P. Lipari, Astropart. Phys. 1 (1993) 195.
[34] E.V. Bugaev et al., Phys. Rev. D 58 (1998) 054001.
[35] M. Thunman, G. Ingelman, P. Gondolo, Astropart. Phys. 5 (1996) 309.
[36] G. Gelmini, P. Gondolo, G. Varieschi, Phys. Rev. D 61 (2000) 036005; Phys. Rev. D 61 (2000) 056011.
[37] J. Ahrens et al., Phys. Rev. D 67 (2003) 012003.
[38] W. Lohmann, R. Kopp, R. Voss, CERN Yellow Report 85-03, 1985.
[39] A. Karle, in: Proceedings of the Workshop on Simulation and Analysis Methods for Large Neutrino Telescopes, DESY-PROC-1999-01, 1999, p. 174.
[40] S. Hundermark, in: Proceedings of the Workshop on Simulation and Analysis Methods for Large Neutrino Telescopes, DESY-PROC-1999-01, 1999, p. 276.
[41] S. Hundertmark, Ph.D. thesis, Humboldt-Universität zu Berlin, 1999.
[42] V.J. Stenger, DUMAND internal Report HDC-1-90, 1990.
[43] J. Ahrens et al., NIM, submitted.
[44] C. Wiebusch, in: Proceedings of the Workshop on Simulation and Analysis Methods for Large Neutrino Telescopes, DESY-PROC-1999-01, 1999, p. 302.
[45] G.J. Feldman, R.D. Cousins, Phys. Rev. D 57 (1998) 3873.
[46] Y. Fukuda et al., Phys. Rev. Lett. 81 (1998) 1562.
[47] Q.R. Ahmad et al., Phys. Rev. Lett. 87 (2001) 071301.
[48] E. Waxman, J. Bahcall, Phys. Rev. D 59 (1999) 023002.
[49] K. Mannheim, R.J. Protheroe, J.P. Rachen, Phys. Rev. D 63 (2001) 023003.
[50] F.W. Stecker, M.H. Salamon, Space Sci. Rev. 75 (1996) 341.
[51] E. Waxman, Nucl. Phys. Proc. Suppl. 118 (2003) 353. Available from <astro-ph/0211358>.
[52] J. Ahrens et al., Astrophys. J. 583 (2003) 1040.